

ADAPTIVE LARGE EDDY SIMULATION FOR COMPLEX AERODYNAMIC PROBLEMS

Jitesh Rane

Submitted in Partial Fulfillment of the Requirements
for the Degree of

DOCTOR OF PHILOSOPHY

Approved by:
Prof. Onkar Sahni, Chair
Prof. Mark Shephard
Prof. Farhan Gandhi
Prof. Christopher Letchford



Department of Mechanical, Aerospace, and Nuclear Engineering
Rensselaer Polytechnic Institute
Troy, New York

[October 2022]
Submitted October 2022

© Copyright 2022
by
Jitesh Rane
All Rights Reserved

CONTENTS

LIST OF TABLES	v
LIST OF FIGURES	vi
ACKNOWLEDGMENT	viii
ABSTRACT	ix
1. Introduction	1
2. Dynamic Large Eddy Simulation	2
2.1 Combined Model Formulation	2
2.2 Dynamic Procedure	6
2.2.1 Local Variational Germano Identity	6
2.2.2 Local VGI Computation	8
3. VMS based error estimator	10
3.1 General Formulation	10
3.2 Formulation for 1D Advection-Diffusion Equation	12
3.2.1 Generalization of VMS Error Estimator	14
3.2.1.1 Generalization to Multi-dimensional Cases	14
3.2.2 Application to the Navier-Stokes Equations	15
3.2.3 Application to Periodic Problems	15
4. Adaptive Strategies	16
4.1 Baseline/Non-adapted Cases	16
4.1.1 Problem Setup: Surging Airfoils	16
4.1.2 Summary of Baseline Cases	17
4.1.3 Results and Discussion	19
4.1.4 Feature/Vortex Detection and Tracking: LEV	24
4.1.5 Active Reflex Camber	26
4.2 Overview of Adaptive Strategies	32
4.2.1 Zonal Refinement/Adaptation	33
4.2.2 Nodal Size Field-based Adaptation	35
4.2.3 Feature-based Refinement/Adaptation	36
4.2.4 Results using Different Adaptive Strategies	37

5. Results and Discussion: Zonal Based Adaptation/Refinement	46
5.1 Force Response	47
5.2 Flowfield: Spanwise Vorticity	48
5.3 Cp	52
APPENDICES	
A. THIS IS AN APPENDIX	53

LIST OF TABLES

4.1	Summary of cases	17
4.2	Summary of cases	27
4.3	Drag ratios ($\mu_{sect} = 2.0$)	32
4.4	Summary of zonal refinement based meshes	34

LIST OF FIGURES

2.1	1-D schematic of the h - and H -level grids for local VGI	7
4.1	Schematic of the problem	16
4.2	Mesh around the airfoil with refinement zones	18
4.3	Layered and graded mesh around the leading edge and trailing edge of the airfoil	19
4.4	Normalized lift force for $Re=40,000$ (green line with open triangles), $200,000$ (red line with closed circles) and $1,000,000$ (blue line with open circles) at $\mu_{sect}=1.0$ and 1.2	19
4.5	Spanwise vorticity at 8 different phases for $Re=40,000$ (left column), $200,000$ (middle column) and $1,000,000$ (right column) at $\mu_{sect} = 1.0$	21
4.6	Spanwise vorticity at 8 different phases for $Re=40,000$ (left column), $200,000$ (middle column) and $1,000,000$ (right column) at $\mu_{sect} = 1.2$	23
4.7	LEV size for $Re=40,000$ (green line with open triangles), $200,000$ (red line with closed circles) and $1,000,000$ (blue line with open circles) at $\mu_{sect}=1.0$ and 1.2	25
4.8	LEV position (with respect to the leading edge of the airfoil) for $Re=40,000$ (green line with open triangles), $200,000$ (red line with closed circles) and $1,000,000$ (blue line with open circles) at $\mu_{sect}=1.0$ and 1.2	26
4.9	Variation of \tilde{U}_{rel} at $\mu_{sect} = 1.5$ (green solid line) and 2.0 (blue dashed line), open circles on each curve represent the portion of the oscillation cycle when reflex camber is activated	27
4.10	Mesh around the airfoil for the non-actuated and actuated cases during the reverse flow region	28
4.11	Instantaneous spanwise vorticity at 4 different phases for the non-actuated (left column) and actuated (right column) cases at $\mu_{sect} = 2.0$	30
4.12	Normalized total drag in the reverse flow region for the non-actuated (blue with open circles) and actuated (red with open triangles) cases at $\mu_{sect} = 2.0$	31
4.13	Mesh and error-field for zonal based refinement strategy	34
4.14	Mesh and estimated error for size-based refinement strategy (Ms_a1)	35
4.15	Mesh and error-field for feature based strategy	37
4.16	Normalized forces for different meshes	38

4.17	Spanwise vorticity comparison at $\psi = 195^\circ$ for different meshes	40
4.18	Spanwise vorticity comparison at $\psi = 210^\circ$ for different meshes	41
4.19	Spanwise vorticity comparison at $\psi = 270^\circ$ for different meshes	42
4.20	C_p comparison for different meshes. Top surface C_p is denoted by solid lines and bottom surface C_p is denoted by dashed lines	44
5.1	Normalized forces for different meshes	47
5.2	Spanwise vorticity comparison at $\psi = 180^\circ$ for different meshes	48
5.3	Spanwise vorticity comparison at $\psi = 210^\circ$ for different meshes	49
5.4	Spanwise vorticity comparison at $\psi = 240^\circ$ for different meshes	50
5.5	Spanwise vorticity comparison at $\psi = 270^\circ$ for different meshes	51
5.6	C_p comparison for different meshes. Top surface C_p is denoted by solid lines and bottom surface C_p is denoted by dashed lines	52

ACKNOWLEDGMENT

ABSTRACT

CHAPTER 1

Introduction

CHAPTER 2

Dynamic Large Eddy Simulation

2.1 Combined Model Formulation

This work uses the incompressible Navier Stokes equations in the arbitrary Lagrangian Eulerian (ALE) description. The strong form of the equations is given as

$$\begin{aligned} u_{k,k} &= 0 \\ u_{i,t} + (u_j - u_j^m)u_{i,j} &= -p_{,i} + \tau_{ij,j}^\nu + f_i \end{aligned} \tag{2.1}$$

where u_i is the velocity vector, u_i^m is the mesh velocity vector, p is the pressure (scaled by the constant density), $\tau_{ij}^\nu = 2\nu S_{ij}$ is the symmetric (Newtonian) viscous stress tensor (scaled by the density), ν is the kinematic viscosity, $S_{ij} = 0.5(u_{i,j} + u_{j,i})$ is the strain-rate tensor, and f_i is the body force vector (per unit mass). Note that Einstein summation notation is used.

The weak form is stated as follows: find $\mathbf{u} \in \mathcal{S}$ and $p \in \mathcal{P}$ such that

$$\begin{aligned} B(\{w_i, q\}, \{u_i, p\}; u_l^m) &= \int_{\Omega} [w_i(u_{i,t} + u_i u_{j,j}^m) + w_{i,j}(-u_i(u_j - u_j^m) + \tau_{ij}^\nu - p\delta_{ij}) - q_{,k}u_k] d\Omega \\ &\quad + \int_{\Gamma_h} [w_i(u_i(u_j - u_j^m) - \tau_{ij}^\nu + p\delta_{ij})n_j + qu_k n_k] d\Gamma_h \\ &= \int_{\Omega} w_i f_i d\Omega \end{aligned} \tag{2.2}$$

for all $\mathbf{w} \in \mathcal{W}$ and $q \in \mathcal{P}$. \mathcal{S} and \mathcal{P} are suitable trial/solution spaces and \mathcal{W} is the test/weight space. \mathbf{w} and q are the weight functions for the velocity and pressure variables, respectively. Ω is the spatial domain and Γ_h is the portion of the domain boundary with Neumann or natural boundary conditions.

The above weak form can be written concisely as: find $\mathbf{U} \in \mathcal{U}$ such that

$$B(\mathbf{W}, \mathbf{U}; u_l^m) = (\mathbf{W}, \mathbf{F}) \quad (2.3)$$

for all $\mathbf{W} = [\mathbf{w}, q]^T \in \mathcal{V}$. $\mathbf{U} = [\mathbf{u}, p]^T$ is the vector of unknown solution variables and $\mathbf{F} = [\mathbf{f}, 0]^T$ is the source vector. The solution and weight spaces are: $\mathcal{U} = \{\mathbf{U} = [\mathbf{u}, q]^T | \mathbf{u} \in \mathcal{S}; q \in \mathcal{P}\}$ and $\mathcal{V} = \{\mathbf{W} = [\mathbf{w}, q]^T | \mathbf{w} \in \mathcal{W}; q \in \mathcal{P}\}$, respectively.

Throughout this text $B(\cdot, \cdot)$ is used to represent the semi-linear form that is linear in its first argument and (\cdot, \cdot) is used to denote the L_2 inner product. $B(\mathbf{W}, \mathbf{U}; u_l^m)$ is split into bilinear and semi-linear terms as shown below.

$$B(\mathbf{W}, \mathbf{U}; u_l^m) = B_1(\mathbf{W}, \mathbf{U}; u_l^m) + B_2(\mathbf{W}, \mathbf{U}) = (\mathbf{W}, \mathbf{F}) \quad (2.4)$$

where $B_1(\mathbf{W}, \mathbf{U}; u_l^m)$ contains the bilinear terms and $B_2(\mathbf{W}, \mathbf{U})$ consists of the semi-linear terms. These are defined as

$$\begin{aligned} B_1(\mathbf{W}, \mathbf{U}; u_l^m) &= \int_{\Omega} [w_i(u_{i,t} + u_i u_{j,j}^m) + w_{i,j}(u_i u_j^m + \tau_{ij}^\nu - p \delta_{ij}) - q_{,k} u_k] d\Omega \\ &\quad + \int_{\Gamma_h} [w_i(-u_i u_j^m - \tau_{ij}^\nu + p \delta_{ij}) n_j + q u_k n_k] d\Gamma_h \end{aligned} \quad (2.5)$$

$$B_2(\mathbf{W}, \mathbf{U}) = - \int_{\Omega} w_{i,j} u_i u_j d\Omega + \int_{\Gamma_h} w_i u_i u_j n_j d\Gamma_h \quad (2.6)$$

The Galerkin weak form is obtained by considering the finite-dimensional or discrete solution spaces $\mathcal{S}^h \subset \mathcal{S}$ and $\mathcal{P}^h \subset \mathcal{P}$ and the weight space $\mathcal{W}^h \subset \mathcal{W}$, where the superscript h is used as a mesh parameter to denote discretized spaces and variables in a finite element context. Using these spaces, $\mathcal{U}^h = \{\mathbf{U}^h = [\mathbf{u}^h, p^h]^T | \mathbf{u}^h \in \mathcal{S}^h; p^h \in \mathcal{P}^h\}$ and $\mathcal{V}^h = \{\mathbf{W}^h = [\mathbf{w}^h, q^h]^T | \mathbf{w}^h \in \mathcal{W}^h; q^h \in \mathcal{P}^h\}$ are defined. The Galerkin weak form is then stated concisely as: find $\mathbf{U}^h \in \mathcal{U}^h$ such that

$$B(\mathbf{W}^h, \mathbf{U}^h) = (\mathbf{W}^h, \mathbf{F}) \quad (2.7)$$

for all $\mathbf{W}^h \in \mathcal{V}^h$. Note for brevity we have dropped u_l^m term in the arguments of the semi-linear form. The Galerkin weak formulation corresponds to a method for direct numerical

simulation since no modeling is employed. However, when the finite-dimensional spaces are incapable of representing the fine/small scales, the Galerkin formulation yields an inaccurate solution. A model term is added to overcome this difficulty, e.g., as done in the residual-based variational multiscale (RBVMS) formulation.

In RBVMS, a set of model terms is added to the Galerkin weak form that results in the following variational formulation: find $\mathbf{U}^h \in \mathcal{U}^h$ such that

$$B(\mathbf{W}^h, \mathbf{U}^h) + M_{rbvms}(\mathbf{W}^h, \mathbf{U}^h) = (\mathbf{W}^h, \mathbf{F}) \quad (2.8)$$

for all $\mathbf{W}^h \in \mathcal{V}^h$. M_{rbvms} represents the set of model terms due to the RBVMS approach.

A scale separation is used to decompose the solution and weight spaces as $\mathcal{S} = \mathcal{S}^h \oplus \mathcal{S}'$ and $\mathcal{P} = \mathcal{P}^h \oplus \mathcal{P}'$, and $\mathcal{W} = \mathcal{W}^h \oplus \mathcal{W}'$, respectively. Thus, the solution and weight functions are decomposed as $u_i = u_i^h + u'_i$ and $p = p^h + p'$ or $\mathbf{U} = \mathbf{U}^h + \mathbf{U}'$, and $w_i = w_i^h + w'_i$ and $q = q^h + q'$ or $\mathbf{W} = \mathbf{W}^h + \mathbf{W}'$, respectively. Note that coarse-scale or resolved quantities are denoted by $(\cdot)^h$ and fine-scale or unresolved quantities by $(\cdot)'$. The coarse-scale quantities are resolved by the grid whereas the effects of the fine scales on the coarse scales are modeled. In RBVMS, the fine scales are modeled as a function of the strong-form residual due to the coarse-scale solution. This is represented abstractly as $\mathbf{U}' = \mathcal{F}(\mathbf{R}(\mathbf{U}^h); \mathbf{U}^h)$, where $\mathbf{R}(\cdot) = [\mathbf{R}^m(\cdot), R^c(\cdot)]^T$ is the strong-form residual of the equations with $\mathbf{R}^m(\cdot)$ (or $R_i^m(\cdot)$) and $R^c(\cdot)$ as those of the momentum and continuity equations, respectively. Specifically, the fine-scale quantities are modeled as $u'_i \approx -\tau_M R_i^m(u_k^h, p^h; u_l^m)$ and $p' \approx -\tau_C R^c(u_k^h)$, where τ_C and τ_M are stabilization parameters (e.g., see details in Tran and Sahni [?]). This provides a closure to the coarse-scale problem as it involves coarse-scale solution as the only unknown. This is why $M_{rbvms}(\mathbf{W}^h, \mathbf{U}^h)$ is written only in terms of the unknown coarse-scale solution \mathbf{U}^h . In summary, $M_{rbvms}(\mathbf{W}^h, \mathbf{U}^h)$ can be written as

$$\begin{aligned}
M_{rbvms}(\mathbf{W}^h, \mathbf{U}^h) = & \\
& \sum_e \int_{\Omega_e^h} \underbrace{[-(w_i^h u_{j,j}^m + w_{i,j}^h u_j^m) \tau_M R_i^m(u_k^h, p^h; u_l^m)]}_{M_{rbvms}^{ALE}(\mathbf{W}^h, \mathbf{U}^h)} \\
& + \underbrace{q_{,i}^h \tau_M R_i^m(u_k^h, p^h; u_l^m)}_{M_{rbvms}^{cont}(\mathbf{W}^h, \mathbf{U}^h)} + \underbrace{w_{i,j}^h \tau_C R^c(u_k^h) \delta_{ij}}_{M_{rbvms}^P(\mathbf{W}^h, \mathbf{U}^h)} \\
& + \underbrace{w_{i,j}^h (u_i^h \tau_M R_j^m(u_k^h, p^h; u_l^m) + \tau_M R_i^m(u_k^h, p^h; u_l^m) u_j^h)}_{M_{rbvms}^C(\mathbf{W}^h, \mathbf{U}^h)} \\
& - \underbrace{w_{i,j}^h \tau_M R_i^m(u_k^h, p^h; u_l^m) \tau_M R_j^m(u_k^h, p^h)}_{M_{rbvms}^R(\mathbf{W}^h, \mathbf{U}^h)} d\Omega_e^h
\end{aligned} \tag{2.9}$$

Note that all model terms are written in terms of the resolved scales within each element (where e denotes an element and contributions from all elements are summed). The last model term is used to represent the Reynolds stresses (i.e., M_{rbvms}^R) while the two terms prior to it are used to represent the cross-stress terms (i.e., M_{rbvms}^C).

In previous studies [?, ?], it was found that the RBVMS model provides a good approximation for the turbulent dissipation due to the cross stresses but the dissipation due to the Reynolds stresses is underpredicted and turns out to be insufficient. Therefore, a combined subgrid-scale model was employed which uses the RBVMS model for the cross-stress terms and the dynamic Smagorinsky eddy-viscosity model for the Reynolds stress terms. This was done in both a finite element code [?, ?] and a spectral code [?]. The combined subgrid-scale model is defined as

$$B(\mathbf{W}^h, \mathbf{U}^h) + M_{comb}(\mathbf{W}^h, \mathbf{U}^h; C_S, h) = (\mathbf{W}^h, \mathbf{F}) \tag{2.10}$$

where

$$\begin{aligned}
M_{comb}(\mathbf{W}^h, \mathbf{U}^h; C_S, h) = & M_{rbvms}^{ALE}(\mathbf{W}^h, \mathbf{U}^h) + M_{rbvms}^{cont}(\mathbf{W}^h, \mathbf{U}^h) \\
& + M_{rbvms}^P(\mathbf{W}^h, \mathbf{U}^h) + M_{rbvms}^C(\mathbf{W}^h, \mathbf{U}^h) \\
& + (1 - \gamma) M_{rbvms}^R(\mathbf{W}^h, \mathbf{U}^h) \\
& + \gamma M_{smag}^R(\mathbf{W}^h, \mathbf{U}^h; C_S, h)
\end{aligned} \tag{2.11}$$

$$M_{smag}^R(\mathbf{W}^h, \mathbf{U}^h; C_S, h) = \int_{\Omega} w_{i,j}^h 2 \underbrace{(C_S h)^2 |S^h|}_{\nu_t} S_{ij}^h d\Omega \quad (2.12)$$

where ν_t is the eddy viscosity, $|S^h|$ is the norm of the strain-rate tensor (i.e., $|S^h| = \sqrt{2\mathbf{S}^h : \mathbf{S}^h} = \sqrt{2S_{ij}^h S_{ij}^h}$), h is the local mesh size, and C_S is the Smagorinsky parameter. The parameter γ is set to be either 0 or 1 in order to control which model is used for the Reynolds stresses. Note that $\gamma = 0$ results in the original RBVMS model and $\gamma = 1$ results in the combined subgrid-scale model. In this study, $\gamma = 1$ is employed. The Smagorinsky parameter is computed dynamically in a local fashion as discussed below.

2.2 Dynamic Procedure

To dynamically compute the Smagorinsky parameter in a local fashion, we follow the localized version of the variational Germano identity (VGI) developed by Tran *et al.* [?]. In this procedure, Lagrangian averaging along fluid pathtubes is applied to make it robust and which maintains the localized nature of the VGI. The dynamic local procedure and the associated approximations are summarized in this section.

2.2.1 Local Variational Germano Identity

The VGI involves comparing the variational form (including the model terms) between different levels of the discretization such that they are nested. In the localized version of the VGI, a set of nested spaces are constructed by using a series of coarser second-level grids along with the primary or original grid. We refer to the primary grid as the h -grid and any grid in the series of second-level grids as the H -level grid. Each H -level grid is chosen such that it is associated with an interior node in the primary grid. This is done such that each H -grid is identical to the h -grid except that the given node k in the h -grid is coarsened or removed resulting in a nested H -level grid for node k , which we refer to as the H_k -grid. Note that each H_k -grid involves local coarsening around a given node k while the remainder of the mesh remains the same. This is demonstrated in 1-D in Figure 2.1, where Ω^{H_k} is the macro element in the H_k -grid corresponding to node k while Ω^{P_k} is the corresponding patch of elements around node k in the h -grid. Note that $k = 1, 2, \dots, n_{intr}$, where n_{intr} is the number of interior nodes in the h -grid. Therefore, there are n_{intr} grids at the H level, each of which is paired with the primary h -grid. This results in the following spaces for each

interior node, $\mathcal{U}^{H_k} \subset \mathcal{U}^h \subset \mathcal{U}$ and $\mathcal{V}^{H_k} \subset \mathcal{V}^h \subset \mathcal{V}$, for the solution and weight functions, respectively.

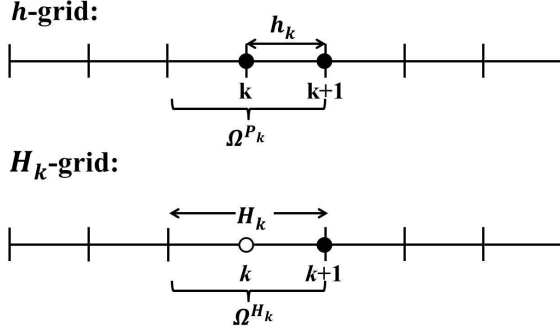


Figure 2.1: 1-D schematic of the h - and H -level grids for local VGI

The local VGI procedure then uses the H_k -grids with the h -grid to compute the model parameter at every node k in the h -grid. By setting $\mathbf{W}^h = \mathbf{W}^{H_k}$, since $\mathcal{V}^{H_k} \subset \mathcal{V}^h \subset \mathcal{V}$, we get (for details see Ref. [?]).

$$\begin{aligned} M_{comb}(\mathbf{W}^{H_k}, \mathbf{U}^h; C_S^k, h_k) - M_{comb}(\mathbf{W}^{H_k}, \mathbf{U}^{H_k}; C_S^k, H_k) = \\ -(B(\mathbf{W}^{H_k}, \mathbf{U}^h) - B(\mathbf{W}^{H_k}, \mathbf{U}^{H_k})) \end{aligned} \quad (2.13)$$

We recognize that determining \mathbf{U}^{H_k} for each interior node k involves a grid-level computation or projection (operations which involve looping over the elements of the H_k -grid). This is prohibitive and therefore, a surrogate is considered. \mathbf{U}^{H_k} is approximated within the macro element using a volume-weighted average of \mathbf{U}^h while outside of the macro element the solution is assumed to be the same between the two grid levels. This assumption further bypasses a grid-level computation. This assumption arises from the requirement on the variational multiscale (VMS) method to provide a localization at the element level and the desire to yield nodal exactness at element corners[?]. This leads to $\mathbf{U}^{H_k} \approx \tilde{\mathbf{U}}^{H_k}|_{\Omega^{H_k}} = \mathbb{A}^{H_k}(\mathbf{U}^h)$, where \mathbb{A}^{H_k} is the local averaging operator defined below.

$$\mathbb{A}^{H_k}(f^h) = \frac{1}{|\Omega^{P_k}|} \int_{\Omega_e^h \in \Omega^{P_k}} f^h d\Omega_e^h \quad (2.14)$$

where $|\Omega^{P_k}|$ is the volume of the local patch and Ω_e^h indicates an element in the h -grid.

This choice is only feasible when the spatial derivatives exist on the weight function. In

addition, instead of using $\tilde{\mathbf{U}}^{H_k}$ to compute \mathbf{S}^{H_k} , \mathbf{S}^{H_k} is also approximated within the macro element as $\tilde{\mathbf{S}}^{H_k}|_{\Omega^{H_k}} \approx \mathbb{A}^{H_k}(\mathbf{S}^h)$. Furthermore, among all of the terms in Equation (2.13) not involving the unknown model parameter, the non-linear convective term is found to be dominating[?]. We note that this assumption holds exactly in a spectral setting where all the bilinear terms cancel out between the H - and h -level grids due to the L_2 orthogonality of spectral modes[?]. The local VGI simplifies to

$$\begin{aligned} & - (B_2(\mathbf{W}^{H_k}, \mathbf{U}^h)_{\Omega^{P_k}} - B_2(\mathbf{W}^{H_k}, \tilde{\mathbf{U}}^{H_k})_{\Omega^{H_k}} \\ & M_{smag}(\mathbf{W}^{H_k}, \mathbf{U}^h; C_S^k, h_k)_{\Omega^{P_k}} - M_{smag}(\mathbf{W}^{H_k}, \tilde{\mathbf{U}}^{H_k}; C_S^k, H_k)_{\Omega^{H_k}} \end{aligned} \quad (2.15)$$

Now an appropriate choice for $\mathbf{W}^{H_k} \in \mathcal{V}^{H_k}$ must be made. In a 1D setting, we select $\mathbf{W}^{H_k} = [w_i^{H_k}, 0]^T$ with $w_i^{H_k}$ such that it is linear along a spatial direction within the macro element and is constant or flat outside. Within the macro element, $w_i^{H_k}$ is selected such that

$$w_{i,j}^{H_k} = \frac{1}{|\Omega^{H_k}|} \quad (2.16)$$

where $|\Omega^{H_k}|$ is the volume of the element. This choice of \mathbf{W}^{H_k} is feasible in a multi-D setting and on an unstructured mesh consisting elements of mixed topology, however, a larger patch must be considered. An extra layer of elements is needed around the macro element to attain a constant value in the outside region. This extra layer acts as a buffer region. This choice is made due to its ease of implementation. For more details see Refs. [?].

2.2.2 Local VGI Computation

At this point we drop the subscript k in H_k and P_k and superscript k in C_S^k for brevity and only use it when necessary. The residual of the local VGI is defined as

$$\epsilon_{ij} = L_{ij} - 2(C_S h)^2 M_{ij} \quad (2.17)$$

where

$$L_{ij} = \left(\left(\frac{1}{|\Omega^H|}, u_i^h u_j^h \right)_{\Omega^P} - \left(\frac{1}{|\Omega^H|}, \tilde{u}_i^H \tilde{u}_j^H \right)_{\Omega^H} \right) \quad (2.18)$$

$$M_{ij} = \left(\left(\frac{1}{|\Omega^H|}, |S^h| S_{ij}^h \right)_{\Omega^P} - \left(\frac{H}{h} \right)^2 \left(\frac{1}{|\Omega^H|}, |\tilde{S}^H| \tilde{S}_{ij}^H \right)_{\Omega^H} \right) \quad (2.19)$$

The least squares method is applied to determine the model parameter as follows

$$(C_S h)^2 = \frac{1}{2} \frac{L_{ij} M_{ij}}{M_{ij} M_{ij}} \quad (2.20)$$

Since the local VGI procedure often leads to negative values for $(C_S h)^2$, an averaging scheme is employed to avoid this issue. Specifically, Lagrangian averaging is applied[?]. To do so, two additional advection-relaxation scalar equations are solved. These are shown in Equations (2.21) and (2.22). The scalars I_{LM} and I_{MM} in these equations are the Lagrangian-averaged counterparts of $L_{ij} M_{ij}$ and $M_{ij} M_{ij}$, respectively.

$$I_{LM,t} + (u_j - u_j^m) I_{LM,j} = \frac{1}{T} (L_{ij} M_{ij} - I_{LM}) \quad (2.21)$$

$$I_{MM,t} + (u_j - u_j^m) I_{MM,j} = \frac{1}{T} (M_{ij} M_{ij} - I_{MM}) \quad (2.22)$$

where T is the timescale over which averaging is applied. Additionally, a local volume-weighted averaging is also applied separately to the numerator and denominator of Equation (2.20) as follows

$$(C_S h)^2 = \frac{1}{2} \frac{\mathbb{A}^H(I_{LM})}{\mathbb{A}^H(I_{MM})} \quad (2.23)$$

where, as before, \mathbb{A}^H represents a local averaging operator. This is equivalent to averaging over local pathtubes[?, ?] and maintains the utility of the local VGI.

CHAPTER 3

VMS based error estimator

In this work, we focus on controlling the spatial discretization error through an *a posteriori* error estimate. Ideally, *a posteriori* error estimate must provide pointwise the exact error, $e^{exact} = u - u^h$, where u is the exact solution and u^h is the numerical approximation u , since knowing how the error varies over space allows us to better choose our spatial discretization. Of course, knowledge of the exact error implies knowledge of the true solution rendering the simulation pointless. Therefore, we employ an approximate error estimate $\|e\|_*$ measured in some norm of interest such as the L^2 norm, H^1 norm, or H^1 semi-norm. We would like that the the error estimate has a local representation over an element k and bounds (from above) the exact error.

Many estimators, both explicit and implicit, have been developed and studied in the literature (e.g. see books by Ainsworth and Oden [?], Verfürth [?]). More recently, progress has been made in obtaining reliable explicit error estimates for the Navier-Stokes equations through the variational multi-scale approach (e.g. Hauke, Fuster, and Lizarraga [?]). We employ the VMS-based error estimator since the VMS framework is currently used for LES and it is computationally inexpensive.

We first review the general formulation of the VMS approach. We then discuss the error estimator based on the VMS approach for a model 1D advection-diffusion problem followed by how it can be extended to a multi-dimensional setting. We then extend the VMS-based error estimator to the Navier-Stokes equations and periodic problems of interest.

3.1 General Formulation

The VMS paradigm relies on the idea of decomposing spaces of interest into coarse-scale and fine-scale subspaces. The coarse-scale space represents our choice of spatial discretization and is therefore finite dimensional, whereas the fine-scale space encompasses the remainder of the space that our discretization cannot represent and is therefore infinite dimensional. More importantly, the fine-scale space is necessarily a representation of the spatial discretization error for the solution space.

Let us specifically consider the trial and weighting spaces for some model finite element

problem as \mathcal{S} and \mathcal{W} , respectively. Let $\bar{\mathcal{S}}$ be a subset of \mathcal{S} and let $\mathcal{P} : \mathcal{S} \rightarrow \bar{\mathcal{S}}$ be a linear projector such that $\mathcal{P}u = \bar{u}$ where $u \in \mathcal{S}$, $\bar{u} \in \bar{\mathcal{S}}$, and $\text{Range}(\mathcal{P}) = \bar{\mathcal{S}}$. This naturally leads to the definition of a complementary space $\mathcal{S}' = \text{Kernel}(\mathcal{P})$ and allows for the direct sum decomposition $\mathcal{S} = \bar{\mathcal{S}} \oplus \mathcal{S}'$ and $\mathcal{W} = \bar{\mathcal{W}} \oplus \mathcal{W}'$, where $\bar{\mathcal{S}}$ and $\bar{\mathcal{W}}$ represent the coarse-scale subspaces and \mathcal{S}' and \mathcal{W}' represent the fine-scale subspaces. $\bar{\mathcal{S}}$ is the same as \mathcal{S}^h and \bar{u} is the same as u^h . This equivalence applies for the coarse-scale weighting space as well. We use the $\bar{\cdot}$ notation in this section to be consistent with the most prevalent literature on VMS-based error estimation (i.e., it is slightly different from the notation used in the previous section).

Because of the direct-sum representation, we can also state that $u = \bar{u} + u'$ is a unique decomposition where $\bar{u} \in \bar{\mathcal{S}}$ and $u' \in \mathcal{S}'$ for any $u \in \mathcal{S}$.

Consider the usual statement of a homogeneous linear partial-differential equation with linear operator \mathcal{L} and forcing function f

$$\mathcal{L}(u) = f \quad u|_{\Gamma} = 0 \quad (3.1)$$

which yields the following finite element problem: find $u \in \mathcal{S}$ such that

$$B(w, u) = (w, f), \quad \forall w \in \mathcal{W} \quad (3.2)$$

where $B(\cdot, \cdot)$ is a bilinear form stemming from integration by parts of Equation 3.1 and (\cdot, \cdot) is the L^2 inner product.

Applying the scale decomposition and leveraging the direct-sum representation yields a coarse-scale problem and a fine-scale problem.

Find $\bar{u} \in \bar{\mathcal{S}}$ such that

$$B(\bar{w}, \bar{u}) + B(\bar{w}, u') = B(\bar{w}, \bar{u}) + (\mathcal{L}^* \bar{w}, u') = (\bar{w}, f), \quad \forall \bar{w} \in \bar{\mathcal{W}} \quad (3.3)$$

Find $u' \in \mathcal{S}'$ such that

$$B(w', \bar{u}) + B(w', u') = (w', \mathcal{L}\bar{u}) + B(w', u') = (w', f), \quad \forall w' \in \mathcal{W}' \quad (3.4)$$

The coarse-scale problem is coupled with the fine-scale problem through u' , which again is conveniently also a representation of the discretization error. A further remark is that the coarse-scale problem has the form of a stabilized finite element method once a substitution

for the form of u' is made. The fine-scale problem does afford a solution (see Hughes and Sangalli [?]), where

$$u'(y_i) = - \int_{\Omega} g'(x_i, y_i)(\mathcal{L}\bar{u} - f)(x_i) d\Omega \quad (3.5)$$

where $g'(x_i, y_i)$ is the fine-scale Green's function with $x_i, y_i \in \Omega$, which is not known in general, except for certain cases - one of which is the 1D linear advection-diffusion equation. Since the Navier-Stokes equations have advective and diffusive properties, we use the 1D linear advection-diffusion as a starting point to derive the a posteriori error estimator.

One final remark is that the form of the fine-scale Green's function is directly tied to the choice of projector \mathcal{P} . This equivalently also means that the various choices of \mathcal{P} leads to different unique pairings of u and u' . Hughes and Sangalli [?] explored two options for the \mathcal{P} : \mathcal{P}_{L^2} and \mathcal{P}_{H^1} , and found that for 1D advection-diffusion systems, the \mathcal{P}_{H^1} led to a localization of g' to single elements and led to an optimal solution for \bar{u} in the H_0^1 -norm or H^1 -seminorm, making this choice a practical one. The localization of g' is ideal for constructing local error estimators.

3.2 Formulation for 1D Advection-Diffusion Equation

The steady advection-diffusion equation with the strong form given by: find the scalar ψ such that

$$\mathcal{L}(\psi) = a_i \psi_{,i} - \kappa \psi_{,ii} = f \quad (3.6)$$

where a_i is an advection vector, κ is the diffusivity constant and f is a forcing function. We can define the corresponding spaces for the solution and weighting functions as usual

$$\mathcal{S}_\psi = \{v | v \in H^1(\Omega)^N, v = g \text{ on } \Gamma_g\} \quad (3.7)$$

$$\mathcal{W}_\psi = \{w | w \in H^1(\Omega)^N, w = 0 \text{ on } \Gamma_g\} \quad (3.8)$$

The corresponding weak form is given by: find $\psi \in \mathcal{S}_\psi$ such that

$$\int_{\Omega} \left[w_{\psi} a_i \psi_{,i} + \kappa w_{\psi,i} \psi_{,i} \right] d\Omega - \int_{\Gamma_h} \kappa w_{\psi} \psi_{,i} n_i d\Gamma_h = \int_{\Omega} w_{\psi} f d\Omega, \quad \forall w_{\psi} \in \mathcal{W}_{\psi} \quad (3.9)$$

Equation 3.5 describes the relationship between the coarse-scale solution $\bar{\psi}$ and the discretization error. The strong residual acts as a local source for error and the fine-scale Green's function distributes it over the spatial domain. From Equation 3.5, we can define the H^1 -seminorm over an element

$$|e_k^{\psi}|_* = |e_k^{\psi}|_{H^1(\Omega_k^h)} = |\psi'_k|_{H^1(\Omega_k^h)} = |(\mathcal{R}(\bar{\psi}_k))| \left\| \int_{\Omega_k^h} g'_{,i} d\Omega_k^h \right\|_{L^2(\Omega_k^h)} \quad (3.10)$$

where $\mathcal{R}(\bar{\psi}) = \mathcal{L}(\bar{\psi}) - f = \mathcal{L}(\psi^h) - f$ is constant for piecewise linear finite elements with piecewise constant input data and material properties. We focus on the H^1 -seminorm in particular since we want to control the error in the gradients in the solution field.

For the 1D advection-diffusion equation, the fine-scale Green's function has an analytical form (see Hauke, Doweidar, and Miana [?]) that is used to attain the following simplified form

$$\|\psi'_k\|_{H^1(\Omega_k^h)} = \nu_{k,1D}^{err} |\mathcal{R}(\bar{\psi}_k)| \sqrt{|\Omega_k^h|} \quad (3.11)$$

$$= \nu_{k,1D}^{err} \|\mathcal{R}(\bar{\psi}_k)\|_{L^2(\Omega_k^h)} \quad (3.12)$$

where $\nu_{k,1D}^{err} = \frac{1}{|a_i|} \sqrt{Pe_h \coth(Pe_h) - 1}$ and $Pe_h = \frac{h_k |a_i|}{2\kappa}$ is the cell-Peclet number, and h_k denotes a local mesh size.

Note that this is an explicit expression which does not require solving additional differential equations (local or global) like implicit error estimators. This makes Equation 3.12 inexpensive to evaluate, although limited in scope to the one-dimensional case. The effectiveness of the VMS based error estimator was tested for a series of cell Peclet numbers Pe_h by Zhang [?] and showed that across all cases, the VMS error estimator provides the exact error in 1D. This is expected since the VMS theory in 1D linear, steady advection-diffusion case makes no assumptions or approximations.

3.2.1 Generalization of VMS Error Estimator

3.2.1.1 Generalization to Multi-dimensional Cases

The primary component of Equation 3.12 that is one-dimensional is the parameter $\nu_{e,1D}^{err}$ because it is not immediately obvious how to choose h_k , the element mesh size, for multi-dimensional anisotropic elements. This problem is equivalent to the problem found when generalizing the 1D stabilization expressions that are used in stabilized finite element methods for advection-diffusion equations to multi-dimensional problems [?] and can therefore be addressed with a similar approach.

For advective-diffusive systems, there are two element-sizes of interest - one corresponding to the direction of local advection and the other corresponding to diffusion. This is reflected in the asymptotes for the exact expression for $\nu_{k,1D}^{err}$. The magnitude of the local advection relative to the local mesh size $\frac{|a_i|}{h_k/2}$ can be represented with $\sqrt{a_i g_{ij} a_j}$ as $g_{ij} = \left(\frac{2}{h_k}\right)^2$ in 1D. For the diffusive length-scale, the metric tensor intrinsically represents an average mesh size for an element so $g_{ij} g_{ij}$ provides a convenient choice. This leads to the final generalized result for ν_k^{err}

$$\nu_k^{err} = \frac{1}{\sqrt{\kappa \sqrt{a_i g_{ij} a_j}} + 3\kappa^2 \sqrt{g_{ij} g_{ij}}} \quad (3.13)$$

and the subsequent final form of the a posteriori error estimator

$$|e_k^\psi|_{H^1(\Omega_k^h)} = |\psi'_k|_{H^1(\Omega_k^h)} \approx \nu_k^{err} \|\mathcal{R}(\bar{\psi}_k)\|_{L^2(\Omega_k^h)} \quad (3.14)$$

The effectivity of the VMS-based error estimator in 2D was tested by Zhang [?] for a 2D advection-diffusion problem. For this multi-dimensional case, it is reported that the error estimator does not exactly capture the true error. Instead, for a wide-range of Pe_h the global effectivity was slightly greater than unity. For $Pe_h = 100$, the effectivity was approximately 1.1, which indicates that the error estimator is slightly overestimating the true error. Note that an effectivity above 1 implies a more conservative error estimator. For an advection-diffusion-reaction problem with a similar Pe_h , Ainsworth et al. [?] reports an effectivity of $\mathcal{O}(50)$ using the equilibrated residual method, which suggests that the VMS-based error estimator performs well.

3.2.2 Application to the Navier-Stokes Equations

As discussed previously, the Navier-Stokes equations possess advective and diffusive properties and extending the stabilization expressions from the 1D advection-diffusion to 3D Navier-Stokes have been effective in previous work. We follow the same path for applying Equation 3.14 to each momentum component of the Navier-Stokes equations and arrive at the following

$$|\mathbf{e}^{NS}|_{H^1(\Omega^h)}^2 = \sum_i |e_i^{NS}|_{H^1(\Omega_k^h)}^2 \quad (3.15)$$

$$|e_i^{NS}|_{H^1(\Omega_k^h)} = |u'_i|_{H^1(\Omega_k^h)} \approx \nu_k^{err,NS} \left\| \mathcal{R}_i^{NS}(\bar{u}_k) \right\|_{L^2(\Omega_k^h)} \quad (3.16)$$

$$\nu_k^{err,NS} = \frac{1}{\sqrt{\nu \sqrt{\bar{u}_i g_{ij} \bar{u}_j} + 3\nu^2 \sqrt{g_{ij} g_{ij}}}} \quad (3.17)$$

$$(3.18)$$

which uses the momentum residual $R_i^{NS}(\bar{u}) = R_i^{NS}(u^h)$.

The discretization error resulting from the continuity equation is ignored since it is generally insignificant compared to the momentum discretization error.

3.2.3 Application to Periodic Problems

We are also interested in applying the VMS-based error estimator to periodic problems in space and/or time. The specific problem of interest in this case is flow over a surging airfoil. In this case, an airfoil oscillates sinusoidally in a constant freestream and is also periodic in the spanwise direction. The mesh for this case is first generated as a 2D/in-plane mesh (i.e., on the front surface), and then extrusion is applied in the spanwise direction. Currently, an adapted mesh is constructed for the entire surging cycle since we are interested in turbulent flows with resolution of fine-scale structures/fluctuations and adapting at different time steps over an oscillation cycle can be computationally expensive. Thus, the VMS-based error estimator is applied to multiple or all time instances/phases over the surging cycle, and the maximum local/elemental error over the surging cycle is chosen. Similarly, for a spanwise extruded mesh, the maximum local/elemental error in the spanwise direction over the extruded-stack of elements is selected.

CHAPTER 4

Adaptive Strategies

In this section, we focus on adaptive LES of flow over a surging airfoil at different conditions. Problem setup, and baseline results including vortex detection and tracking, are first presented using the non-adapted mesh. We also present active flow control cases in the form of active reflex camber. Next, we present the three adaptive strategies and corresponding results.

4.1 Baseline/Non-adapted Cases

4.1.1 Problem Setup: Surging Airfoils

A schematic of the problem setup is shown in Figure 4.1, where U_∞ is the free-stream or mean velocity and α is the angle of attack.

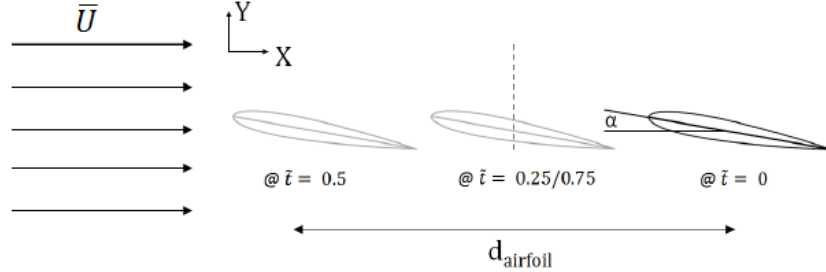


Figure 4.1: Schematic of the problem

The airfoil motion is set as follows

$$d_{airfoil} = A \cos(2\pi f t) = A \cos(2\pi t/T) = A \cos(2\pi \tilde{t}) \quad (4.1)$$

where A is the amplitude and $T = 1/f$ is the time period of the oscillation. The variable \tilde{t} is the fractional part in the oscillation cycle and is defined as $\tilde{t} = \{t/T\} = t/T - \lfloor t/T \rfloor$ (where $\lfloor \cdot \rfloor$ is the floor function).

The (non-dimensional) relative velocity is expressed as

$$\tilde{U}_{rel} = U_{rel}/U_\infty = 1 - U_{airfoil}/U_\infty = (1 + \mu_{sect} \sin(2\pi \tilde{t})) \quad (4.2)$$

where μ_{sect} is the sectional advance ratio. Note that for an advance ratio above 1.0 a negative relative velocity or a reversed flow condition is attained. Under this condition the relative flow is from the (geometric) trailing edge to the leading edge of the airfoil.

At $\tilde{t}=0$, with $\psi=0^\circ$ or $\psi=0^\circ$ (where, ψ is the phase in the oscillation cycle and ψ is the azimuthal position of the blade), the relative velocity is the free-stream velocity (i.e., U_∞). The same holds at $\tilde{t}=0.5$ or $\psi=180^\circ$. At $\tilde{t}=0.25$ or $\psi=90^\circ$, the airfoil is at the maximum relative velocity and at $\tilde{t}=0.75$ or $\psi=270^\circ$ is at the minimum relative velocity. Advancing phase is defined between $\tilde{t}=0$ or $\psi=0^\circ$ and $\tilde{t}=0.5$ or $\psi=180^\circ$ while retreating phase is between $\tilde{t}=0.5$ or $\psi=180^\circ$ and $\tilde{t}=1.0$ or $\psi=360^\circ$ (or back to $\psi=0^\circ$).

The free-stream or mean Reynolds number is defined as $Re = U_\infty C / \nu$, where C is the chord. The reduced frequency is defined as $k = \pi f C / U_\infty$ while the amplitude is related as $A = \frac{\mu_{sect} C}{2k}$.

4.1.2 Summary of Baseline Cases

In the current study, the reduced frequency is held fixed at $k=0.133$ while three Reynolds numbers of $Re=40,000$, $200,000$ and $1,000,000$ are considered together with two advance ratios of $\mu_{sect}=1.0$ and 1.2 , i.e., six cases are considered in total. The angle of attack of the airfoil is set to 6° . Note that we considered the Reynolds number of $Re=40,000$ in previous study [?] that was selected in accordance with the experiments conducted in [?] where the airfoil was placed in a constant flow and oscillated in the streamwise direction. The six cases are summarized in Table 4.2.

Table 4.1: Summary of cases

Airfoil	α	k	μ_{sect}	Re
NACA 0012	6°	0.133	{1.0, 1.2}	{40,000, 200,000, 1,000,000}

The computational domain is set to be $100C \times 50C \times 0.2C$. At the inlet, a constant free-stream velocity is applied (note that the airfoil is moved sinusoidally in the streamwise direction). No-slip condition is prescribed on the moving airfoil. The top and bottom surfaces are set as slip walls. Side surfaces in the spanwise direction (i.e., front and back surfaces) are imposed to be periodic. A natural pressure condition is used at the outlet. A second-order implicit time integration scheme, e.g., see[?], is employed with about 1,440 steps in an oscillation cycle.

An unstructured hybrid/boundary layer mesh is used. The mesh is comprised of hex and wedge elements which is generated by first generating a mesh on the front surface and subsequently applying an extrusion in the spanwise direction. This mesh is used for all the baseline cases. Refinement zones are placed around the airfoil to resolve the flow structures of interest, see Figure 4.2 (where three refinement zones are noted). In the finest refinement zone (Z1), mesh size is set to be $C/256$. In the subsequent two zones (Z2 and Z3), it is set to be $C/128$ and $C/64$, respectively. In the spanwise direction, 50 extruded elements are used. A layered and graded mesh (with geometric growth) is used around the airfoil surface, see Figure 4.3. The first layer height is set to be $\mathcal{O}(10^{-5}C)$ such that it is below 1 in wall units for all cases. Similarly, mesh spacing on the airfoil surface in the streamwise and spanwise directions is set to be below 80 and 50 in wall units, respectively. Overall the mesh contains about 6.2 million nodes and 10.8 million elements.

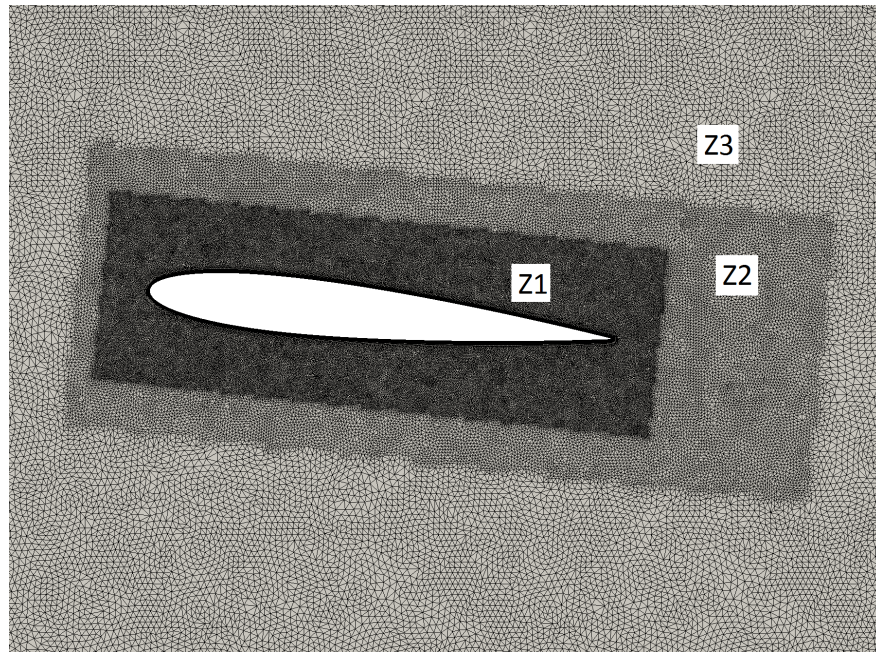


Figure 4.2: Mesh around the airfoil with refinement zones

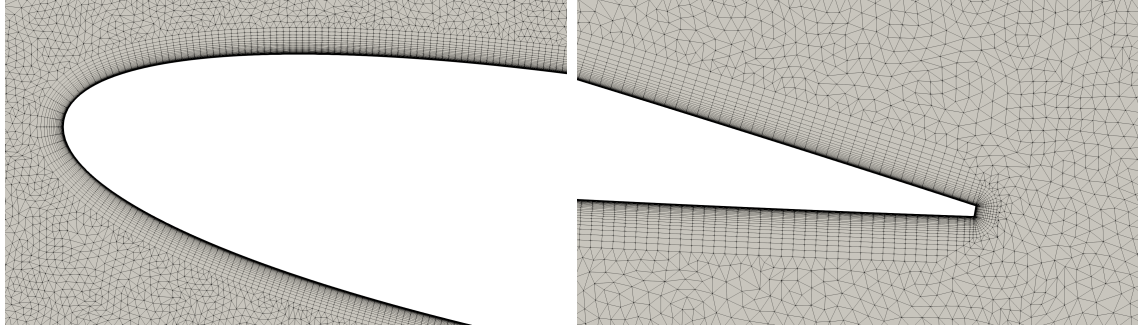


Figure 4.3: Layered and graded mesh around the leading edge and trailing edge of the airfoil

4.1.3 Results and Discussion

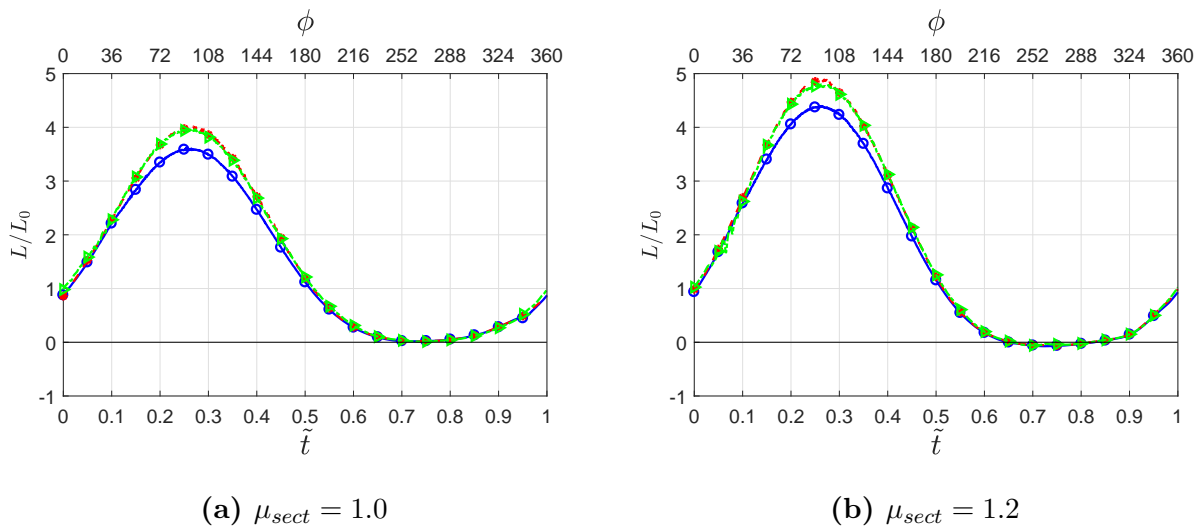


Figure 4.4: Normalized lift force for $Re=40,000$ (green line with open triangles), $200,000$ (red line with closed circles) and $1,000,000$ (blue line with open circles) at $\mu_{sect}=1.0$ and 1.2

Lift force is shown in Figure 4.4. Lift is normalized by its static counterpart, i.e., L_0 is the average or steady lift for the static airfoil at mean Reynolds number. This normalization was used in our previous study with $Re=40,000$ [?] to compare against the experimental data of [?], where a good agreement was shown between the experimental and simulation data. As noted earlier, data is phase averaged over 4 cycles.

Overall, the lift force follows a similar qualitative trend for all the cases. Maximum lift is achieved at $\tilde{t} = 0.25$, which is expected as the airfoil achieves maximum relative velocity at that point. After $\tilde{t} = 0.25$, the lift starts decreasing as the airfoil begins to decelerate and

enters the retreating phase. The lift keeps decreasing till about $\tilde{t} = 0.65$ and plateaus or reaches a value close to zero during the middle of the retreating phase (i.e., around $\tilde{t} = 0.75$ when the airfoil is at its minimum relative velocity). We note that for both advance ratios of $\mu_{sect}=1.0$ and 1.2 a zero relative velocity is attained and for the higher advance ratio of $\mu_{sect}=1.2$ the relative velocity also becomes negative. Lift starts to recover after $\tilde{t} = 0.75$ as the airfoil starts accelerating again. For each advance ratio, the normalized lift during the advancing phase for $Re=1,000,000$ is smaller compared to the other two Reynolds numbers, see Figure 4.4a or Figure 4.4b. The normalized lift is very similar between $Re=40,000$ and 200,000 cases. The peak normalized lift is about 9% lower for the highest Reynolds number case as compared to the lower Reynolds number cases for each advance ratio. On the other hand, for a given Reynolds number the normalized lift is higher for the higher advance ratio, which is expected due to the higher dynamic pressure in any given instance or phase in the surging cycle. The peak normalized lift is about 21% higher for the higher advance ratio case as compared to the lower advance ratio case for each Reynolds number, which is the difference in the peak dynamic pressure between the two advance ratios.

In this section, we present spanwise vorticity over the cycle at 4 different phases of $\psi = 195^\circ, 225^\circ, 270^\circ$, and 330° , which are all in the retreating phase of the surging cycle. We focus our attention on the LEV which is the dominant flow feature. It forms and advects during the retreating phase while in the advancing phase the flow remains attached. As noted earlier, data is phase averaged over 4 cycles. In addition, averaging is also applied in the spanwise direction.

Figure 4.5 shows the spanwise vorticity for the lower advance ratio of $\mu_{sect}=1.0$. The voriticy range is selected to be $[-10,10] \times U_\infty/C$. At $\psi=195^\circ$, the flow over the airfoil is mostly attached, however, the boundary layer is relatively thick as the airfoil is decelerating, see Figures 4.5a, 4.5b and 4.5c. As expected, the boundary layer is much thicker for the lowest Reynolds number of $Re=40,000$ as compared to the other two higher Reynolds number.

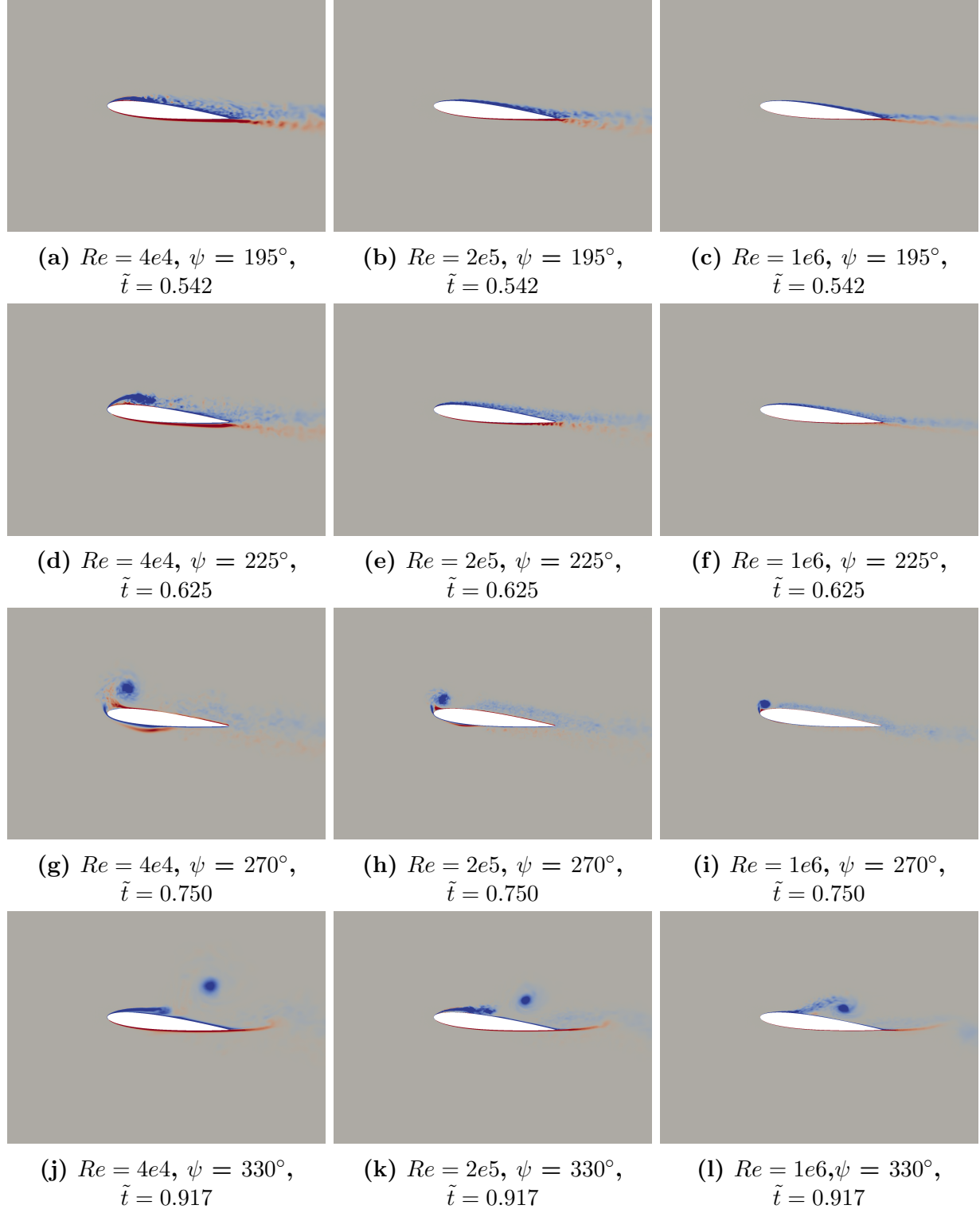


Figure 4.5: Spanwise vorticity at 8 different phases for $Re=40,000$ (left column), $200,000$ (middle column) and $1,000,000$ (right column) at $\mu_{sect} = 1.0$

At $\psi=225^\circ$, the flow is separated near the leading edge for the lowest Reynolds number

of $Re=40,000$ and the separated shear layer rolls up into an LEV, see Figure 4.5e For the other two higher Reynolds number, the flow remains attached. Similarly, at $Re=200,000$ the separated shear layer rolls up into a small LEV at $\psi=240^\circ$, while for $Re=1,000,000$ this occurs at $\psi=270^\circ$ (see Figure 4.5i). As the Reynolds number increases the LEV is formed later in the cycle. In summary, as the airfoil retreats vorticity accumulates around the airfoil and separated shear layer rolls up into a distinct vortex near the leading edge (i.e., an LEV) over the suction or upper side of the airfoil.

In subsequent phases, LEV is ejected into the outer flow and advects. The flow on the suction or upper side reattaches as the leading edge vortex passes over the airfoil. Flow also separates and reattaches on the pressure or lower side, e.g., see marginal flow separation at the trailing edge on the lower side in Fig 4.5d.

It is important to note the differences in LEV evolution with different Reynolds number even though the overall trend of the LEV evolution is similar between different Reynolds number. As already noted, the phase at which the LEV is formed changes with Reynolds number. Further, the size and vertical position of the LEV also changes significantly with Reynolds number. This aspect is discussed in Section 4.1.4.

Figure 4.6 shows the spanwise vorticity for the higher advance ratio of $\mu_{sect}=1.2$. 3 different phases over the retreating phase of the cycle are shown and the range is selected to be $[-10,10] \times U_\infty/C$. As in the $\mu_{sect} = 1.0$ case, at $\psi=195^\circ$ the flow over the airfoil is mostly attached in the $\mu_{sect} = 1.2$ case. As before, the boundary layer is much thicker for the lowest Reynolds number of $Re=40,000$ as compared to the other two higher Reynolds number.

At $\psi=225^\circ$, the flow is fully separated for the lowest Reynolds number of $Re=40,000$ and the separated shear layer is rolled up into an LEV, see Figure 4.6a. Similarly, at $Re=200,000$ a small LEV is seen at $\psi=225^\circ$ (see Figure 4.6b) while for $Re=1,000,000$ LEV is observed at $\psi=240^\circ$. As before, as the Reynolds number increases the LEV is formed later in the cycle. On the other hand, as the advance ratio increases it is formed earlier in the cycle (for a given Reynolds number). For example, for $Re=1,000,000$, the LEV is formed at an earlier phase for $\mu_{sect} = 1.2$ as compared to $\mu_{sect} = 1.0$. Again, as the airfoil retreats vorticity accumulates and shear layer rolls up into a distinct LEV over the suction or upper side of the airfoil.

In subsequent phases, LEV is ejected into the outer flow and advects while the flow reattaches. However, at the higher advance ratio of $\mu_{sect}=1.2$ the LEV initially moves to

the left past the (geometric) leading edge of the airfoil. This is because at $\mu_{sect}=1.2$ the relative flow velocity becomes negative and a reversed flow condition is reached. Again, it is important to note the differences in LEV evolution with different Reynolds number for the advance ratio of $\mu_{sect} = 1.2$. As already noted, the size, position and phase of formation of LEV changes significantly with Reynolds number. This aspect is discussed further in Section 4.1.4.

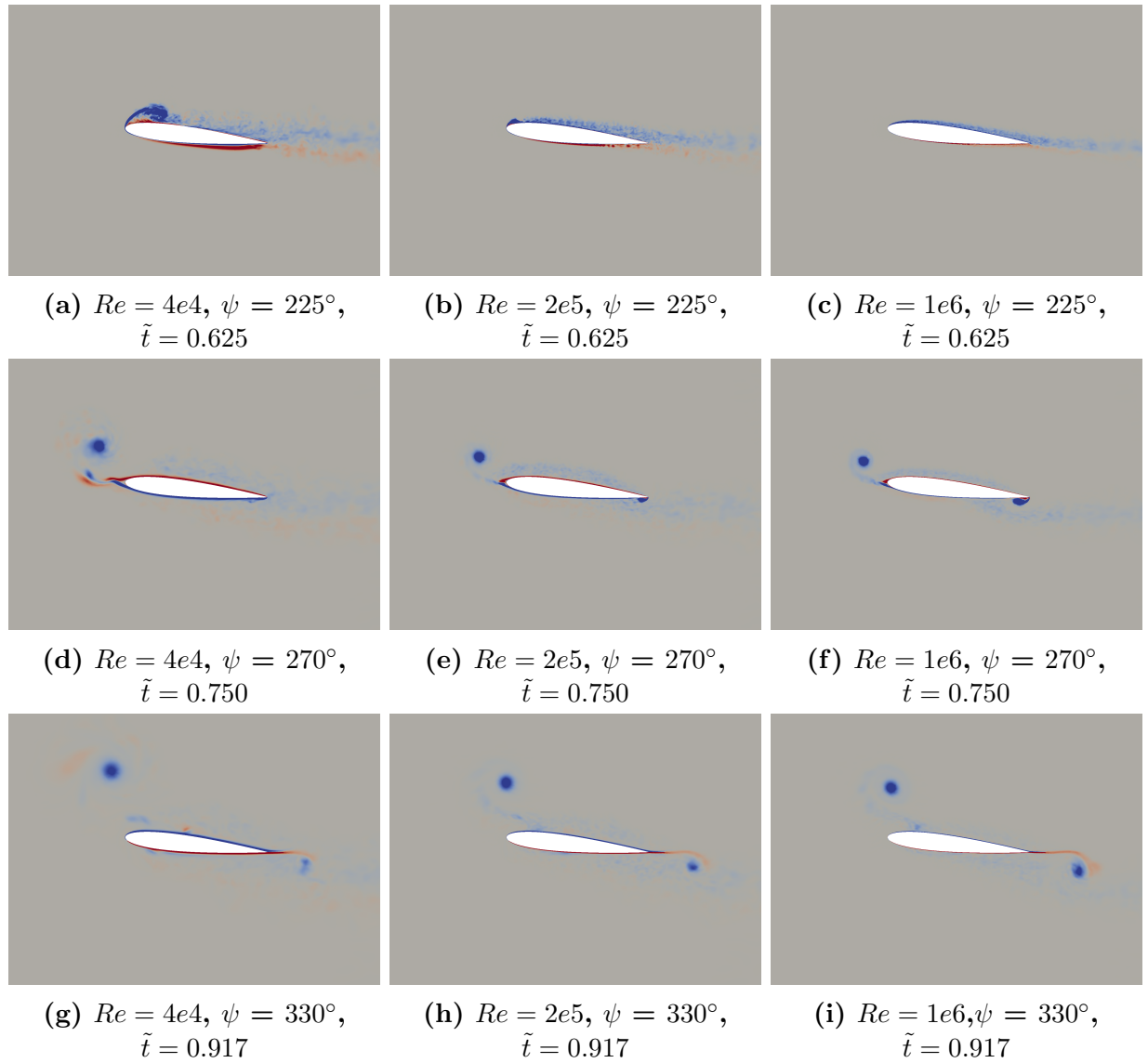


Figure 4.6: Spanwise vorticity at 8 different phases for $Re=40,000$ (left column), $200,000$ (middle column) and $1,000,000$ (right column) at $\mu_{sect} = 1.2$

4.1.4 Feature/Vortex Detection and Tracking: LEV

In this section, we quantify the evolution of the LEV based on its size and position. In order to do so, for each case at first the phase of formation of the LEV is detected and in subsequent phases the LEV is tracked. Pressure and velocity data is analyzed to automatically detect the formation of the LEV. In the retreating portion of the cycle, location with minimum pressure is determined starting at $\psi = 180^\circ$. The first phase at which the minimum pressure location is off the airfoil surface (i.e., away from the airfoil and into the flow) is tagged to be a potential phase for LEV formation. At this potential phase, velocity profile is obtained over multiple lines passing through the minimum pressure location. These are radial lines that are taken at an equispaced interval along the azimuth in the plane of the airfoil (note that the data is averaged in the spanwise direction). Along these lines, at first a relative velocity is computed with respect to the velocity at the minimum pressure location. Subsequently, normal component of the relative velocity is obtained (i.e., normal to each line), which is the azimuthal or tangential component in the polar coordinate system centered around the minimum pressure location. The azimuthal component (of the relative velocity) is analyzed against the velocity profile of a Lamb-Oseen vortex. It is noteworthy that the azimuthal component of the relative velocity along several radial lines at multiple phases in the surging cycle were visually analyzed for different cases and found to fit the Lamb-Oseen vortex model fairly well.

LEV position with respect to the leading edge of the airfoil is presented in Figure 4.8. In the $\mu_{sect} = 1.0$ case, the initial position of the LEV (i.e., position at formation) gets closer to the leading edge as the Reynolds number is increased. Further, LEV remains closest to the airfoil over the cycle for the highest Reynolds number of $Re=1,000,000$ (i.e., note the vertical position of the LEV). On the other hand, LEV initially moves to the left (towards the geometric leading edge) from its initial position for the lowest Reynolds number of $Re=40,000$. In the $\mu_{sect} = 1.2$ case also, similar trends are observed. However, at the higher advance ratio the LEV initially moves to the left past the geometric leading edge for each Reynolds number. This is expected since the relative flow velocity becomes negative (or a reversed flow condition is obtained) at $\mu_{sect} = 1.2$.

Figure 4.7 presents the size or core radius (r_c) of the LEV for all six cases. We note that in simulations the data was recorded at every $\Delta\psi = 15^\circ$ starting at $\psi=15^\circ$. For each case the LEV is formed at about $\tilde{t} = 0.6$ or later. The LEV size is higher for the lowest Reynolds

number of $Re=40,000$ for both advance ratios of $\mu_{sect}=1.0$ and 1.2. This is expected since the boundary layer is thicker for $Re=40,000$ and the resulting separated shear layer rolls up into a larger LEV. The LEV size is very similar for the other two higher Reynolds numbers at $\mu_{sect}=1.0$ and 1.2. In the $\mu_{sect}=1.0$ case, the LEV increases in size till about $\tilde{t} = 0.75$ to 0.8 and subsequently seem to plateau or increase in size relatively slowly. Towards the end of the cycle, the LEV size is about 8% of the chord for $Re=40,000$ at $\mu_{sect}=1.0$, and about 6% for $Re=200,000$ and 1,000,000 at $\mu_{sect}=1.0$. In the $\mu_{sect}=1.2$ case, the LEV increases in size throughout the cycle and towards the end of the cycle reaches about a similar size as the $\mu_{sect}=1.0$ case for each Reynolds number.

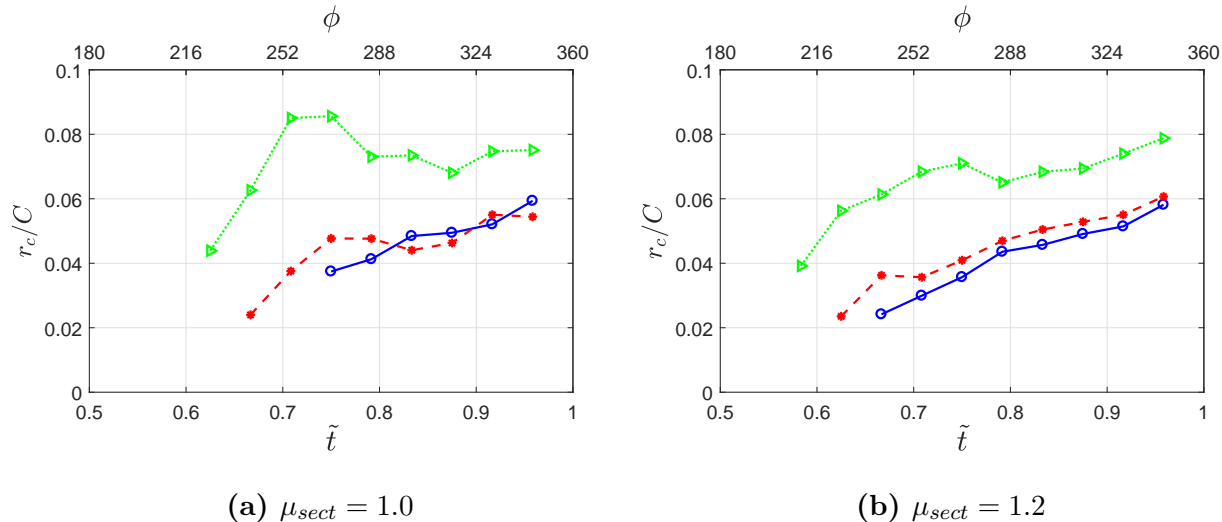


Figure 4.7: LEV size for $Re=40,000$ (green line with open triangles), 200,000 (red line with closed circles) and 1,000,000 (blue line with open circles) at $\mu_{sect}=1.0$ and 1.2

This feature/vortex detection and tracking procedure is useful for feature-based adaptivity, which is discussed in Section 4.2.3.

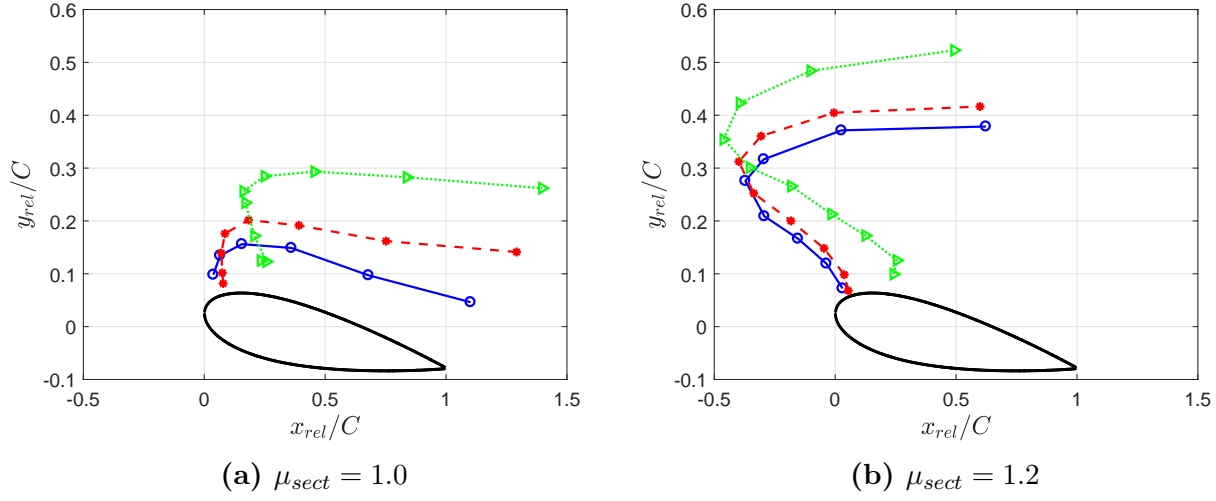


Figure 4.8: LEV position (with respect to the leading edge of the airfoil) for $Re=40,000$ (green line with open triangles), $200,000$ (red line with closed circles) and $1,000,000$ (blue line with open circles) at $\mu_{sect}=1.0$ and 1.2

4.1.5 Active Reflex Camber

In this section, we focus only on high Reynolds number flow ($Re = 1,000,000$) at higher angle of attack of $\alpha = 10^\circ$ and section advance ratios of $\mu_{sect} = 1.5$ and 2.0 . These advance ratios include a significant portion of the retreating phase with negative relative velocity or a reversed flow condition. In this reverse flow condition, massive flow separation near the geometric trailing edge is observed, and as a result, a force is experienced by the airfoil along the surging direction. We try to mitigate this by applying active flow control in the form of active reflex camber.

The case with active reflex camber is referred as the actuated case. In the actuated case, the (geometric) trailing edge is deflected up by an angle of $\beta_{TE}=\alpha=10^\circ$, with the hinge point at the $3/4$ th or 75% chord location (i.e., close to the trailing edge). The reflex camber is applied smoothly over a short period of time (both at activation and deactivation). The full reflex/deflection is achieved just before the reverse flow regime is encountered by the airfoil in the retreating phase, and the airfoil starts to return to its original/undeflected shape once the airfoil is out of the reverse flow.

Figure 4.9 shows the variation of \tilde{U}_{rel} over the cycle at sectional advance ratio of $\mu_{sect} = 1.5$ (blue dashed line) and 2.0 (green solid line). The region with $\tilde{U}_{rel} < 0$ shows the phases when reverse flow is encountered by the airfoil. The open circles on each curve represent the

portion of the oscillation cycle when reflex camber is activated for that particular sectional advance ratio.

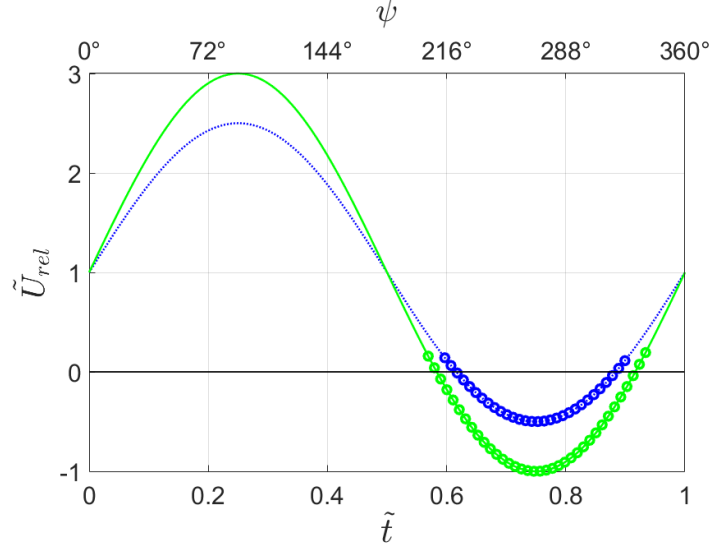


Figure 4.9: Variation of \tilde{U}_{rel} at $\mu_{sect} = 1.5$ (green solid line) and 2.0 (blue dashed line), open circles on each curve represent the portion of the oscillation cycle when reflex camber is activated

Table 4.2 provides a summary of the current cases. $\beta_{TE} = 0$ refers to the non-actuated case while $\beta_{TE} = \alpha$ is the actuated case.

Table 4.2: Summary of cases

Airfoil	α	k	μ_{sect}	Re (mean)	β_{TE}
NACA 0012	10°	0.133	{1.5, 2.0}	1,000,000	{0, α }

The computational domain and boundary conditions for this case are similar to the one mentioned in Section 4.1. Also, as noted earlier, an ALE description is used to account for the motion and deformation of the airfoil. Mesh deformation is currently prescribed based on the motion and deformation of the airfoil. The deformed mesh due to active reflex camber is shown in Figure 4.10.

The computational domain and boundary conditions for this case are similar to the one mentioned in Section 4.1. Also, as noted earlier, an ALE description is used to account for the motion and deformation of the airfoil. Mesh deformation is currently prescribed based

on the motion and deformation of the airfoil. The deformed mesh due to active reflex camber is shown in Figure 4.10.

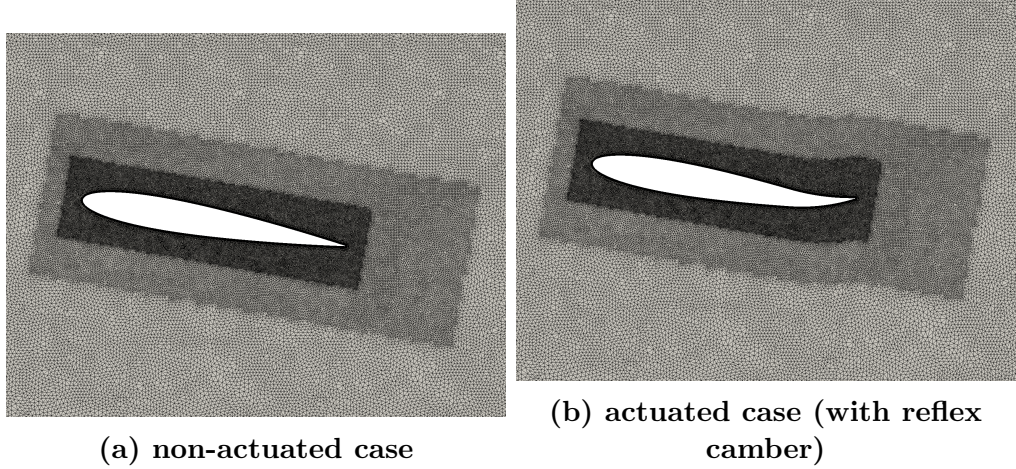


Figure 4.10: Mesh around the airfoil for the non-actuated and actuated cases during the reverse flow region

Instantaneous spanwise vorticity over the oscillation cycle at a few different phases of interest (i.e., in the retreating phase of the cycle) is shown in Figure 4.11 for the higher sectional advance ratio of $\mu_{sect} = 2.0$. We focus our attention on the flow separation near the (geometric) trailing edge region, and note the significant difference in the separated region due to active reflex camber.

Four different phases over the retreating phase of the cycle are shown, and vorticity range is selected to be $[-30,30]U_{sect}/C$. For this advance ratio, the airfoil enters the reverse flow region at $\psi = 210^\circ$, and exits the reverse flow at $\psi = 330^\circ$. Reflex camber is activated at the phase of $\psi=200^\circ$ and reaches the full deflection at $\psi=205^\circ$. After the airfoil exits the reverse flow, the reflexed airfoil starts returning to its undeflected position at $\psi=335^\circ$, and smoothly reaches its original shape at $\psi=340^\circ$.

As the airfoil trailing edge is deflected upwards for this actuated case with $\mu_{sect} = 2.0$, a small vortex is formed near it. Roll up of the boundary layer and LEV formation is seen for both non-actuated and actuated cases at $\psi=210^\circ$. The flow separation near the trailing edge starts to form at the phase of $\psi=225^\circ$.

In the subsequent phases after $\psi=225^\circ$ the size of the separated region increases for the non-actuated case till up to $\psi=285^\circ$. For the actuated case, the separated region is relatively small (see Figures 4.11c and 4.11d) and its size remains fairly constant between

phases $\psi=255^\circ$ and 285° . Overall a significant reduction is observed in the size/extent as well as unsteadiness of the separation bubble near the trailing edge during the reverse flow region due to active reflex camber. The implications of this trailing-edge separated region on the drag force is discussed further below.

After $\psi=285^\circ$, the trailing-edge flow separation begins to wash away from the airfoil for both non-actuated and actuated cases, see Figures 4.11e and 4.11f. For the actuated case at $\psi=345^\circ$, the reflexed trailing edge is at its undeflected position. As the trailing edge is deflected down to its original position, this results in the formation of a small vortex as seen in Figure 4.11h.

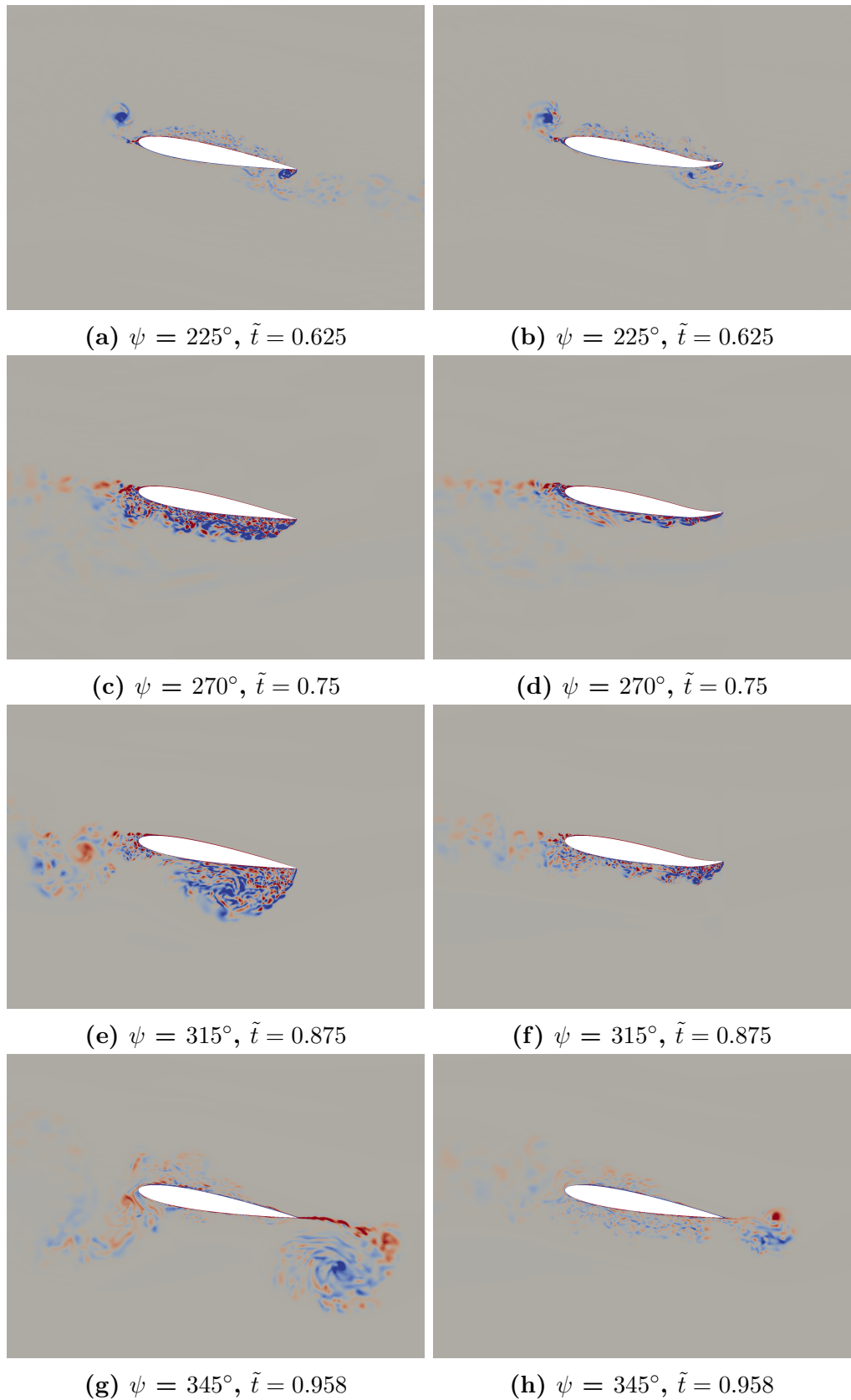


Figure 4.11: Instantaneous spanwise vorticity at 4 different phases for the non-actuated (left column) and actuated (right column) cases at $\mu_{sect} = 2.0$

Figure 4.12 shows the behavior of the total drag in the reverse flow region for the non-actuated and actuated cases at $\mu_{sect} = 2.0$. As before, the total drag is normalized with the total drag of the static case ($\mu_{sect} = 0.0$) at the mean Reynolds number. The drag is negative in the majority of the reverse flow region. For $\mu_{sect} = 2.0$, the reduction in the negative drag due to active reflex camber is significant.

Again, in the non-actuated case the drag fluctuates in the reverse flow region. On the other hand, the drag is fairly monotonic in the actuated case. In the non-actuated case, the drag exhibits a local maximum around $\psi = 220^\circ$ and a local minimum around $\psi = 285^\circ$. The resulting peak-to-peak variation in the non-actuated case is substantial, as shown in Figure 4.12. This peak-to-peak variation in the reverse flow region is mitigated in the actuated case. This is because the trailing-edge separation bubble in the actuated case is substantially smaller and remains fairly constant in size during the reverse flow region, see Figure 4.11.

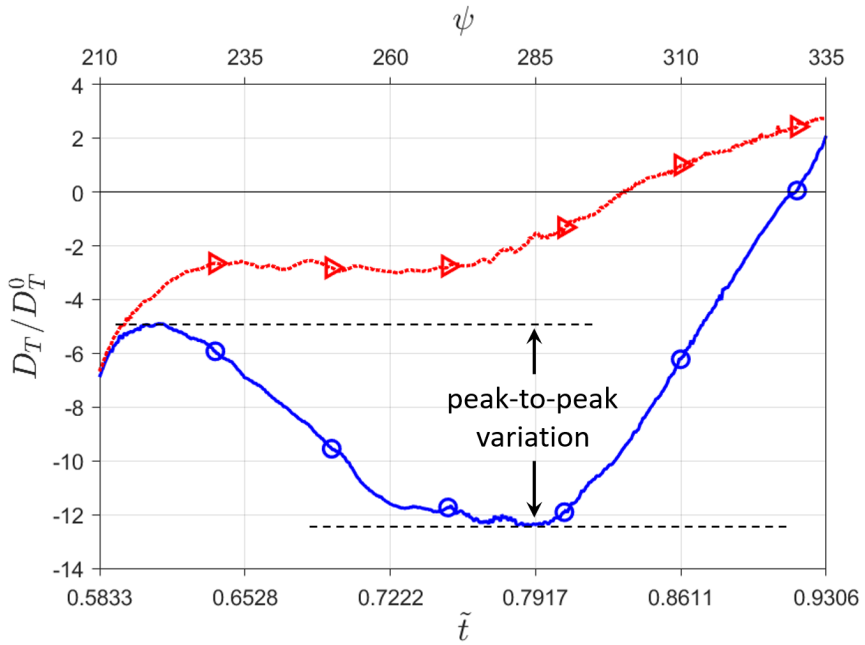


Figure 4.12: Normalized total drag in the reverse flow region for the non-actuated (blue with open circles) and actuated (red with open triangles) cases at $\mu_{sect} = 2.0$

Table 4.3 provides the ratios of the different components of the drag at three phases. At $\psi = 240^\circ$, the total drag in the actuated case is about 0.36 times of the total drag in the

non-actuated case. At $\psi = 255^\circ$ and 270° , the drag ratios are 0.26 and 0.24, respectively. That is we observe a reduction by up to 76% in the total drag. Note that the pressure drag ratios are very similar to the total drag ratios (since at these phases the pressure drag dominates over the viscous drag).

Table 4.3: Drag ratios ($\mu_{sect} = 2.0$)

ψ	$\frac{D_T^{act}}{D_T^{non-act}}$	$\frac{D_p^{act}}{D_p^{non-act}}$	$\frac{D_v^{act}}{D_v^{non-act}}$
240°	0.36	0.35	1.44
255°	0.26	0.24	2.34
270°	0.24	0.22	4.19

4.2 Overview of Adaptive Strategies

In this section, we focus on the low Reynolds number case of $Re = 40,000$ at an angle of attack of $\alpha = 6^\circ$ and advance ratio of $\mu_{sect} = 1.2$. We explore three different adaptation strategies for mesh adaptation based on the VMS-based estimated error.

The first strategy we employ is error estimator based zonal refinement/adaptation. In this strategy, we obtain an initial solution on a baseline mesh for the problem at hand. The VMS-based error estimator is then applied to the solution corresponding to this mesh, and based on the estimated error, the mesh is refined by a factor of 2 in particular zones where high error values are found. Estimated error for this adapted mesh is then calculated, and the mesh is again refined by a factor of 2 in zones of high error. This process is repeated till it is computationally feasible, or a convergence is reached.

The second strategy we employ is fully automated mesh adaptation based on the VMS-based error estimator. In this strategy, the estimated error and a specified target error are used to compute the desired mesh size or resolution in a local fashion, i.e., at every mesh vertex. We refer to this as the nodal size field, and the mesh is refined or coarsened based on this nodal size field.

The third strategy is to employ feature-based refinement/adaptation. This allows for refinement around dominant flow features and also along the path/trajectory of such features, for example, the paths of leading and trailing edge vortices (LEV and TEV) over a surging cycle using vortex tracking. By running an initial simulation, we can get information on the

approximate path that a certain feature will follow, estimate the error along this path, and perform refinement/adaptation along this path.

Further details and applications of these three strategies are included in the following sections.

4.2.1 Zonal Refinement/Adaptation

In this adaptation strategy, an initial solution is obtained on a baseline mesh with basic refinement zones that are usually used for a flow over an airfoil. We refer to this mesh as M0, see Figure 4.13a. For this mesh, the VMS-based error estimator is applied to phase-averaged data, and the maximum error value over all phases and the maximum in the spanwise direction (recall that we use an extruded mesh) for each element is selected to represent the error for that element throughout the surging cycle. The element-level error estimated on this mesh is shown in Figure 4.13b. We can see that higher errors are observed primarily in the region where the LEV traverses through the surging cycle, as well as in the wake of the airfoil. Higher errors are also observed close to the airfoil surface and in the boundary layer mesh region.

Based on estimated error, the mesh is refined by a factor of 2 in zones where high error values are found, including the boundary layer mesh in the streamwise direction. The spanwise resolution is also refined by a factor of 2 (i.e., the number of layers in the spanwise direction is doubled). This mesh, which is referred to as Mz_a1 is shown in Figure 4.13c and the estimated error is shown in Figure 4.13d. It is observed that the error has reduced by a factor of 4 in the Mz_a1 mesh as compared to the M0 mesh. Zonal refinements are added to the Mz_a1 mesh in regions of high error, and the mesh is refined further by a factor of 2 in these zones, along with the boundary layer mesh in the streamwise direction, and the number of layers in the spanwise direction is doubled. This mesh, which is referred to as Mz_a2, is shown in Figure 4.13e. Again, we observe that the error has reduced by a factor of 4 in the Mz_a2 mesh as compared to Mz_a1 mesh.

The number of elements for each mesh is presented in Table 4.4.

Table 4.4: Summary of zonal refinement based meshes

Mesh case	No. of elements
M0	774,525
Mz.a1	2,874,300
Mz.a2	14,329,200

A detailed comparison of results based on these meshes is provided in Section 4.2.4.

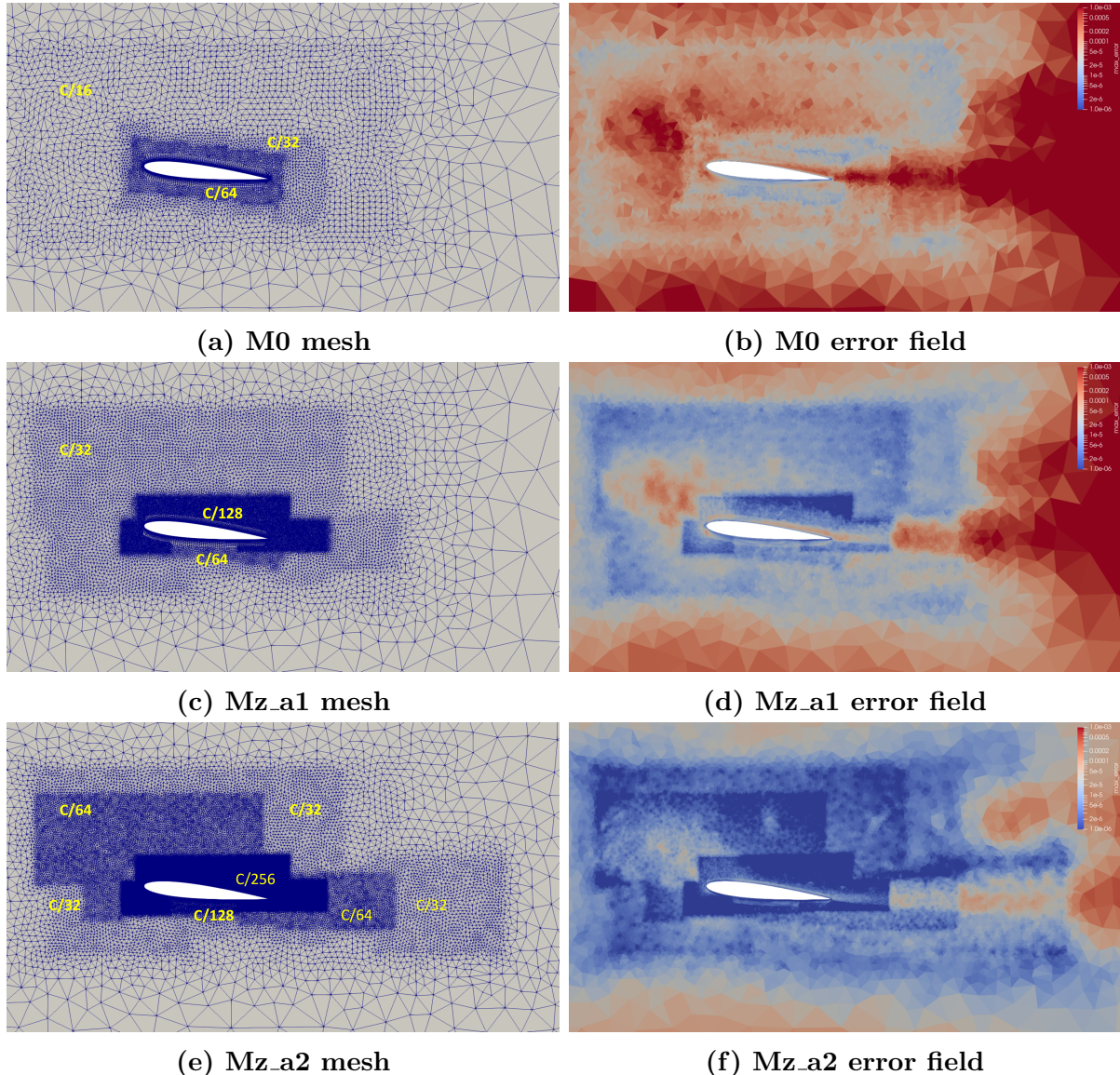


Figure 4.13: Mesh and error-field for zonal based refinement strategy

4.2.2 Nodal Size Field-based Adaptation

In this adaptive strategy, the VMS-based error is calculated on the initial mesh. Based on the estimated error, a nodal size field is calculated using the following equation [?]

$$\frac{e_k}{\tilde{e}_k} = \left(\frac{h_{old}}{h_{new}} \right)^{m+N/2} \quad (4.3)$$

Here, e_k is the measured local error (in the H^1 -seminorm) at an element k , \tilde{e}_k is the target error for an element specified by the user, m is the polynomial order of the approximation space (i.e., $m = 1$ for the linear finite elements used currently), and N is the number of spatial dimensions. h_{old} is current size of the element, and h_{new} is the desired new mesh size. This new mesh size at the element level is assembled at the node/vertex level to perform mesh adaptation.

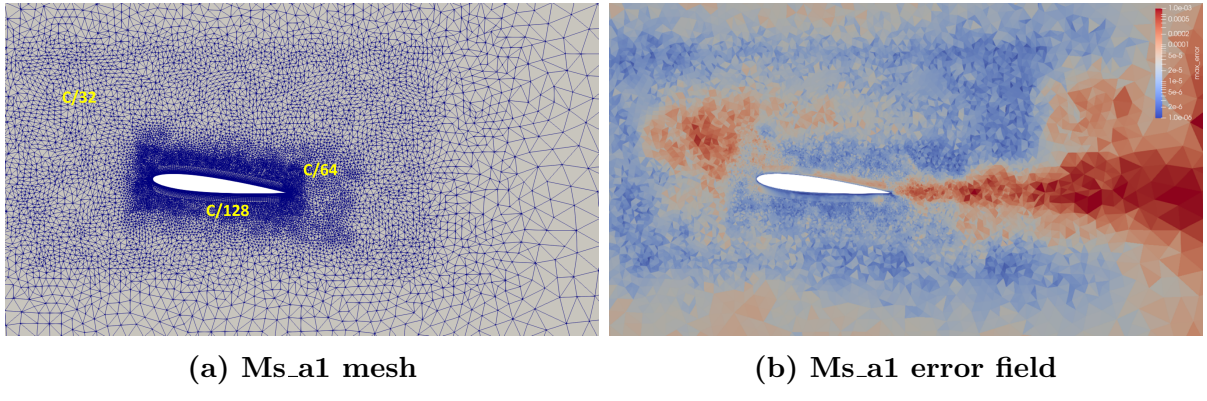


Figure 4.14: Mesh and estimated error for size-based refinement strategy (Ms_a1)

For the surging airfoil case, M0 is used as the initial mesh (Figure 4.13a) and the corresponding error estimated on M0 mesh (Figure 4.13b) is used to calculate h_{new} . The mesh refinement is controlled to have a maximum refinement and maximum coarsening of a factor of 2 to avoid excessive refinement or coarsening in a local region. The mesh obtained using this strategy is shown in Figure 4.14a. Note that in terms of mesh resolution, this mesh compares best against Mz_a1 from zonal refinement strategy. This mesh consists of 2,859,450 elements, which is comparable to 2,874,300 elements for the Mz_a1 mesh. The major differences between the two meshes is that Mz_a1 maintains the same mesh size in various zones, whereas the Ms_a1 mesh is patchy, i.e., a uniform refinement is not maintained within regions of interest. The corresponding estimated error for this mesh is shown in Figure

4.14b. Comparing the estimated error to Mz_a1 mesh, higher error values are observed for Ms_a1 in the LEV region, as well as in the wake of the airfoil. A more thorough comparison of results is mentioned in Section 4.2.4.

4.2.3 Feature-based Refinement/Adaptation

In this strategy, mesh refinement is applied around dominant flow features of interest. In the surging airfoil case, LEV and TEV are the dominant flow features. Using vortex tracking, a path of the dominant vortices is estimated using an initial mesh (M0 in this case). Based on this path, a refinement zone is added around the path of the LEV as well as the TEV. In this feature-based refinement, VMS-based estimated error is used to set the mesh size. In addition, estimated error is also used to refine the mesh around the airfoil in a similar fashion as the error-based zonal refinement discussed earlier. This is done to accurately resolve the flow near the airfoil, including the boundary layer region that plays a direct role in the formation of these dominant vortical structures/features.

Also note that the boundary layer mesh is refined by a factor of 2 in the streamwise direction, and the number of layers in the spanwise direction are doubled as compared to M0. Vortex tracking discussed in Section 4.1.4 is used to estimate the path of the LEV and TEV. The mesh around the path of these vortical features is refined by a factor of 4, to accurately resolve the core of these vortices over its path. The mesh is referred to as Mf_a1 and it contains 3,454,450 elements. This mesh is shown in Figure 4.15a and the estimated error is shown in Figure 4.15b.

Error values along the LEV path are reduced as compared to Ms_a1. Even though the mesh resolution in the LEV region is similar to Mz_a2, higher error is observed as compared to Mz_a2, since the mesh resolution over the airfoil surface is coarser for Mf_a1 as compared to Mz_a2.

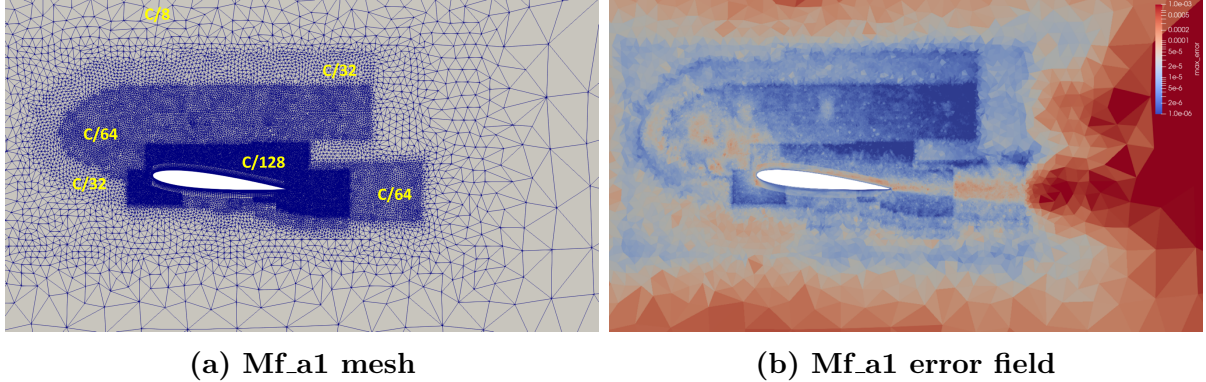


Figure 4.15: Mesh and error-field for feature based strategy

4.2.4 Results using Different Adaptive Strategies

In this section, we compare results for the surging airfoil case based on meshes obtained from different adaptive strategies mentioned above. We compare different quantities of interest. A comparison of force response in the form of normalized lift and drag forces is shown in Figures 4.16a and 4.16b respectively. The normalized lift matches up well for all the meshes considered. Normalized drag shows differences only for Mz_a2 mesh (the finest mesh), specifically between phases $\psi = 160^\circ$ and $\psi = 240^\circ$ whereas the drag response for all the other meshes matches up well.

A comparison of spanwise vorticity for the different meshes is shown in Figures 4.17, 4.18, and 4.19 for phases $\psi = 210^\circ$, $\psi = 225^\circ$, and $\psi = 270^\circ$, respectively. For $\psi = 195^\circ$, as the airfoil is in the retreating phase, boundary layer roll-up towards the geometric leading edge is observed over the airfoil surface. For the meshes based on zonal refinement, as we go from M0 to Mz_a1 and Mz_a2, the separation over the airfoil is well resolved, and more structures are visible as the mesh becomes finer. Comparing Mz_a1, Ms_a1, and Mf_a1 meshes, we can see that Ms_a1 mesh does not capture the fine-scale flow structures as compared to the Mz_a1 mesh, both over the airfoil surface and in the wake of the airfoil. On the other hand, the Mf_a1 mesh captures these fine-scale flow structures.

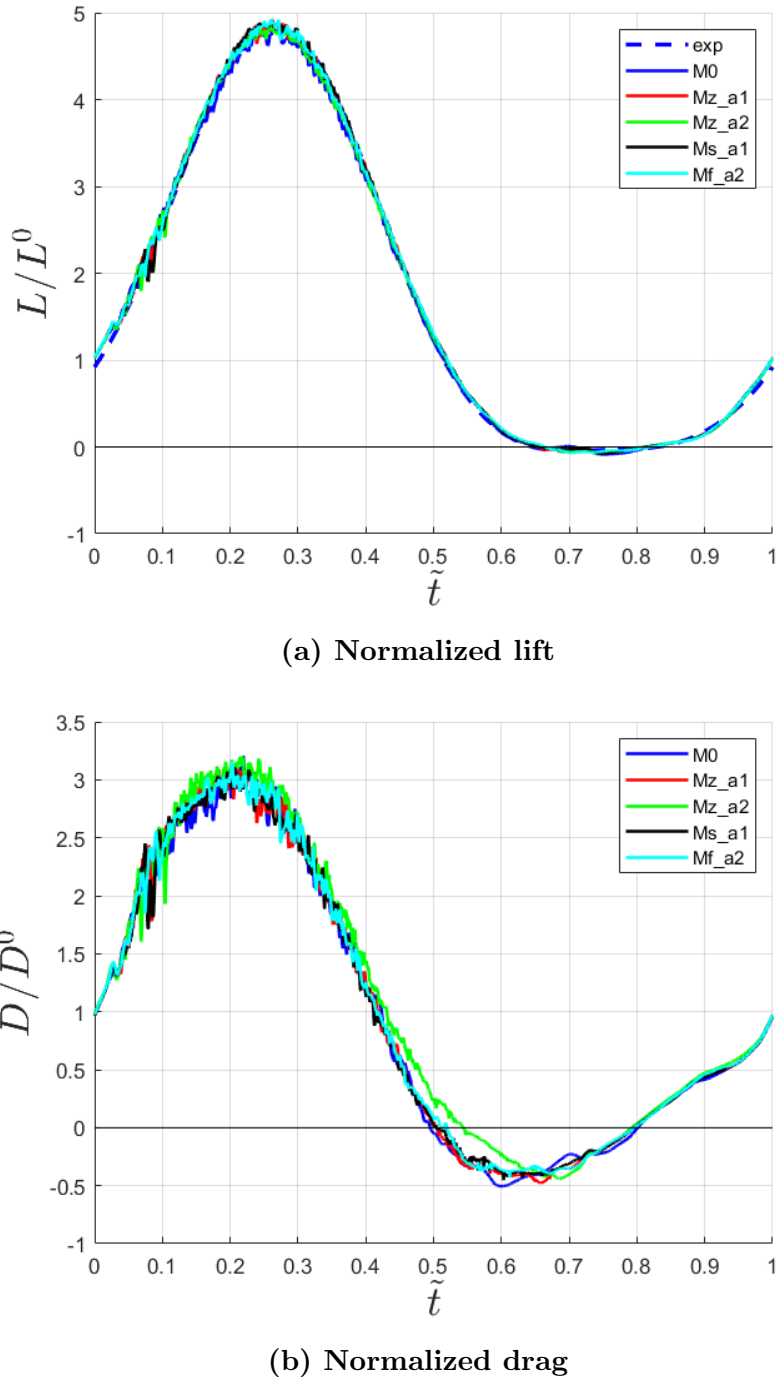


Figure 4.16: Normalized forces for different meshes

For $\psi = 210^\circ$, formation of LEV begins to take place, as we see a distinct vortex build up near the geometric leading edge. At this phase, the differences in the structures resolved by the different meshes become more clear, with Mz_a2 being the most resolved. Similar to $\psi = 195$, the Ms_a1 mesh shows poor resolution of the fine-scale flow structures as compared

to Mz_a1 and Mf_a1 meshes.

For $\psi = 270^\circ$, differences can be seen in the shear layer at the geometric leading edge of the airfoil, and the resolution of the LEV. The LEV and the shear layer are best resolved for Mz_a2 and Mf_a1 meshes. Recall that Mf_a1 is obtained using feature-based mesh refinement designed to resolve the LEV accurately, and has the same mesh resolution as Mz_a2 along the path of the LEV. Once again, shear layer is not well resolved for Ms_a1 as compared to other refined/adapted meshes.

The poor resolution of the flow-field observed for Ms_a1 can be attributed to the mesh not having a uniform refinement in the regions of interest, having been adapted solely based on the error-field obtained, which results in a patchy mesh, i.e., the mesh size does not remain constant in particular zones, and hence, structures are not resolved as desired.

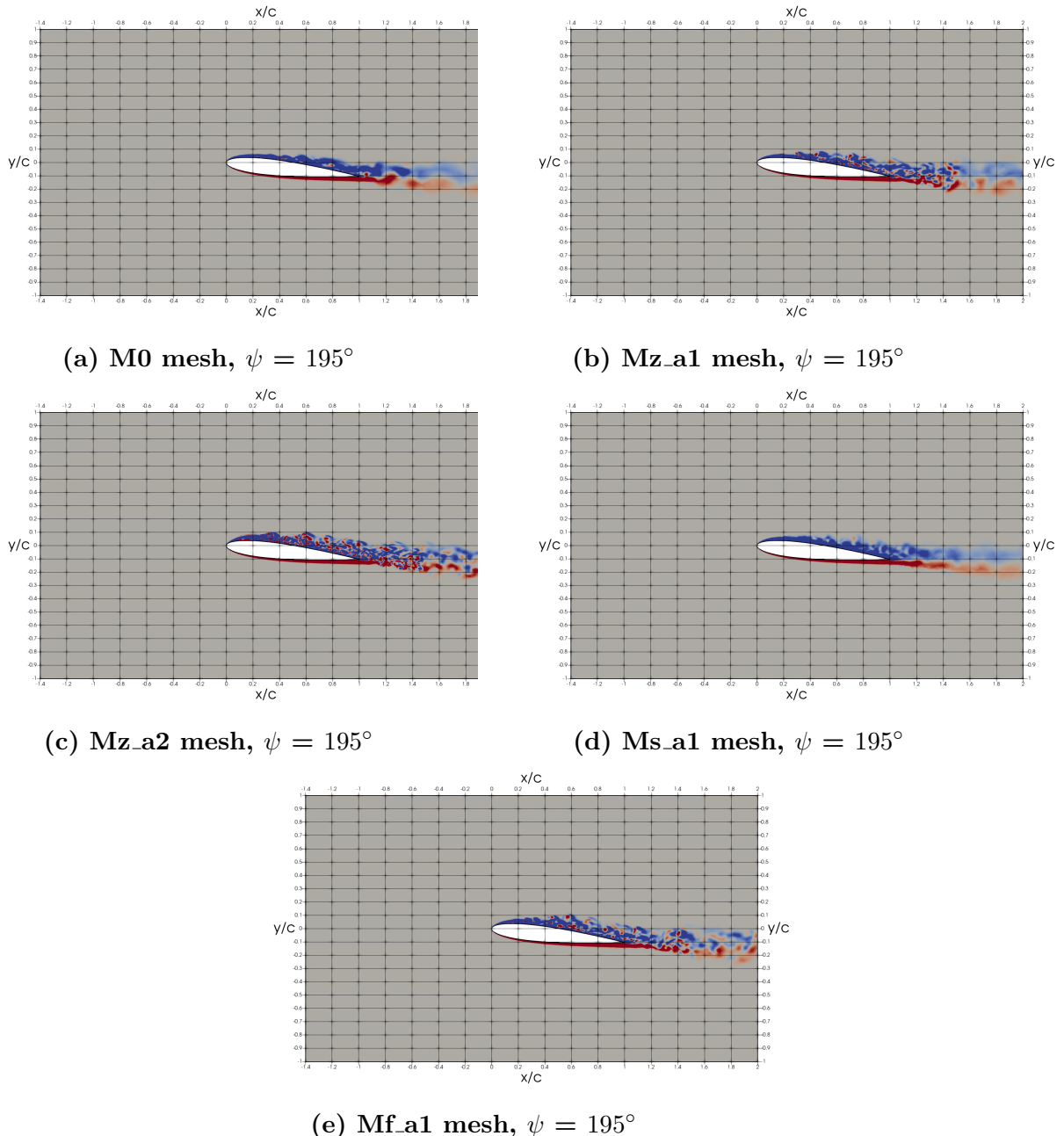


Figure 4.17: Spanwise vorticity comparison at $\psi = 195^\circ$ for different meshes

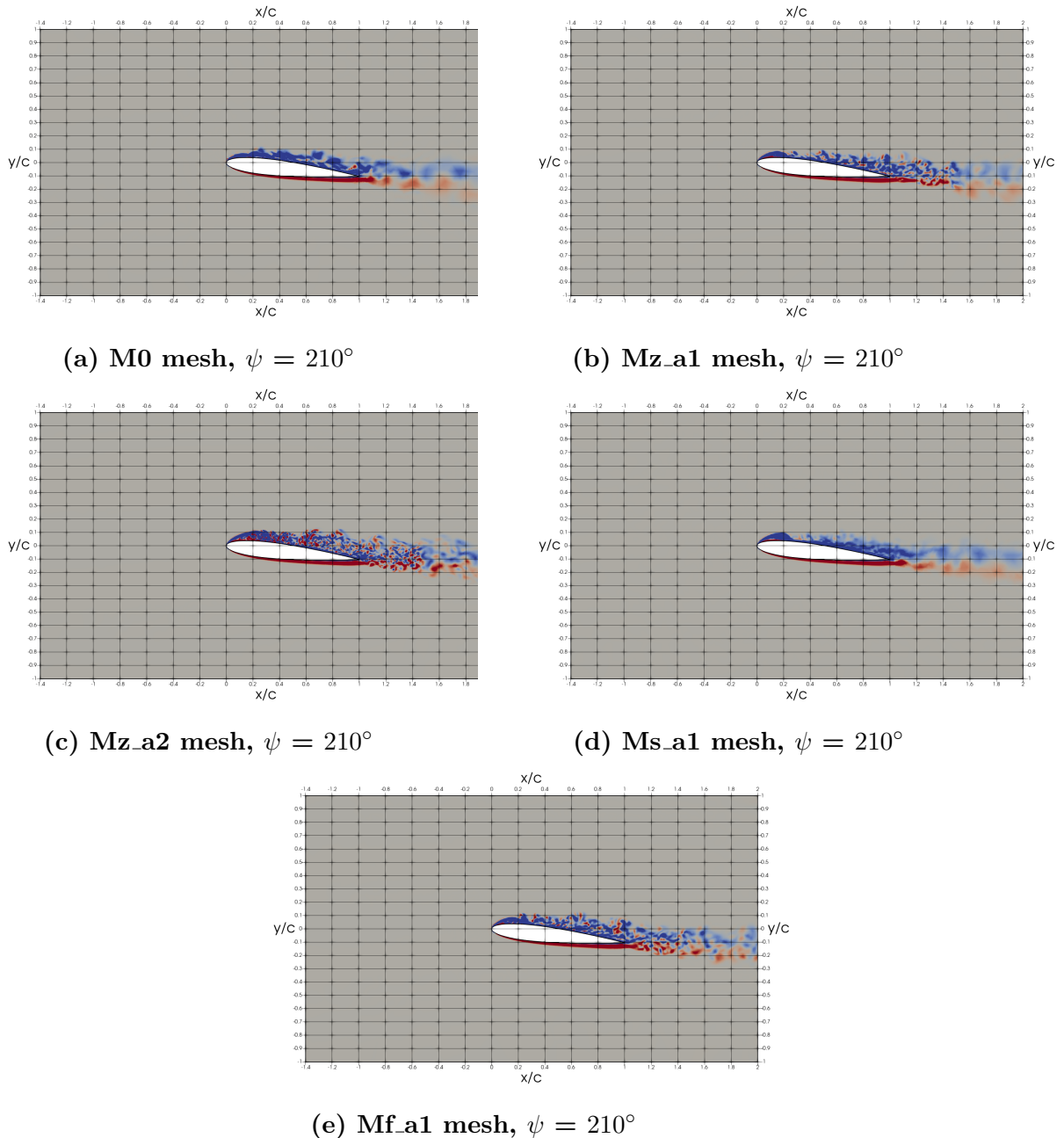


Figure 4.18: Spanwise vorticity comparison at $\psi = 210^\circ$ for different meshes

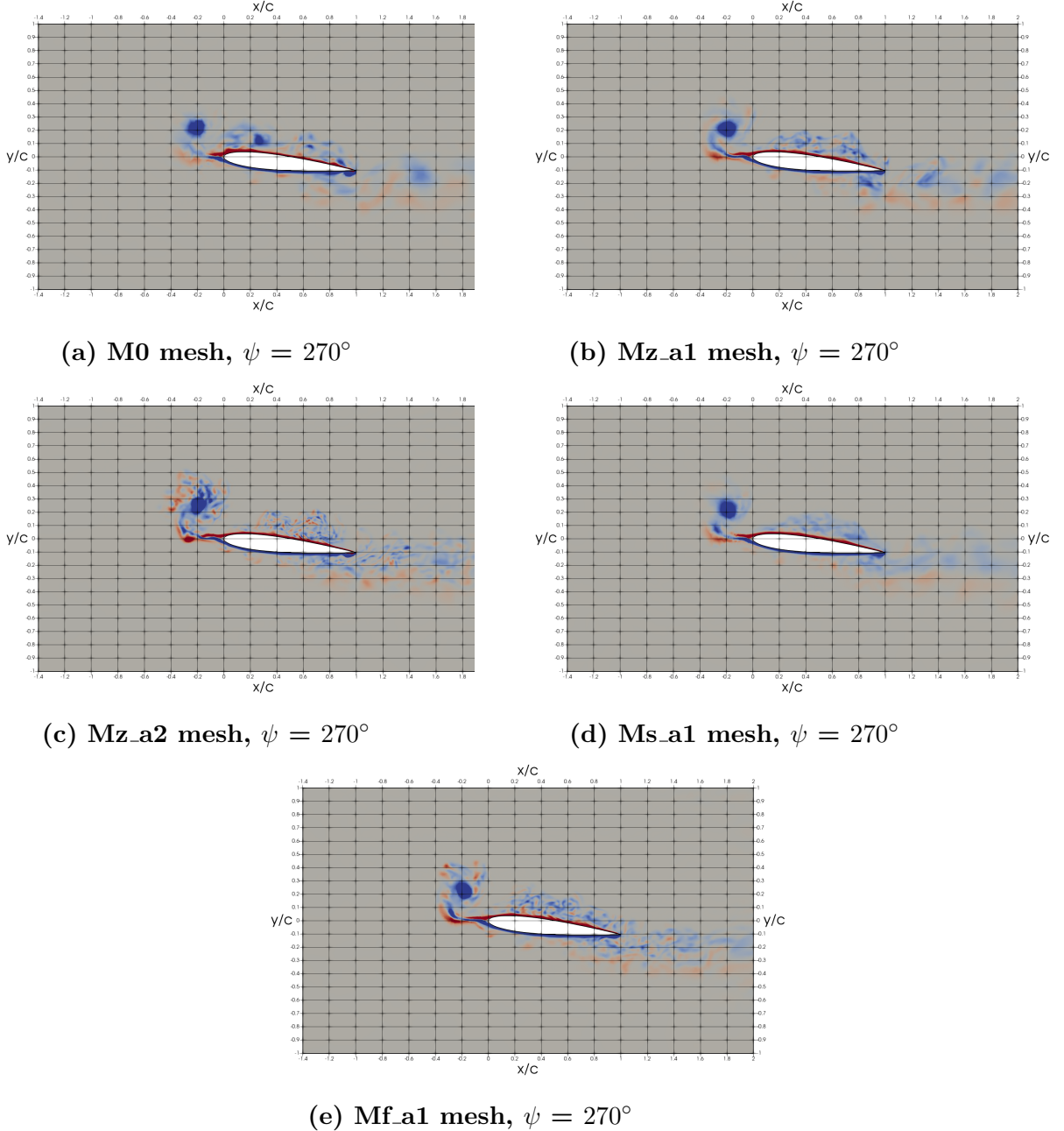


Figure 4.19: Spanwise vorticity comparison at $\psi = 270^\circ$ for different meshes

For a more quantitative comparison, we focus on C_p at different phases of interest leading up to LEV formation. C_p is shown in Figure 4.20 at six phases for all meshes. At $\psi = 180^\circ$, we can see that flow has started to separate for Mz_a2 mesh around $x/c = 0.1$, whereas for all the other meshes, the flow remains attached. For $\psi = 195^\circ$, Mz_a2 and Ms_a1 meshes show clear signs of separation and LEV formation/boundary layer roll-up, whereas the other meshes do not. Although note that the location and C_p curve for Mz_a2 and Ms_a2

meshes are quite different, and separation is detected further downstream for Mz_a2. For $\psi = 210^\circ$, LEV formation is seen for all meshes apart from M0 mesh. $\psi = 225^\circ$ shows LEV formation and flow separation for all meshes, with clear differences in separation location and C_p curve for all the meshes. Note that the y-axis limits vary for different phases to highlight differences in C_p . $\psi = 270^\circ$ and $\psi = 285^\circ$ also show differences in C_p at the geometric trailing edge when the trailing edge vortex starts forming.

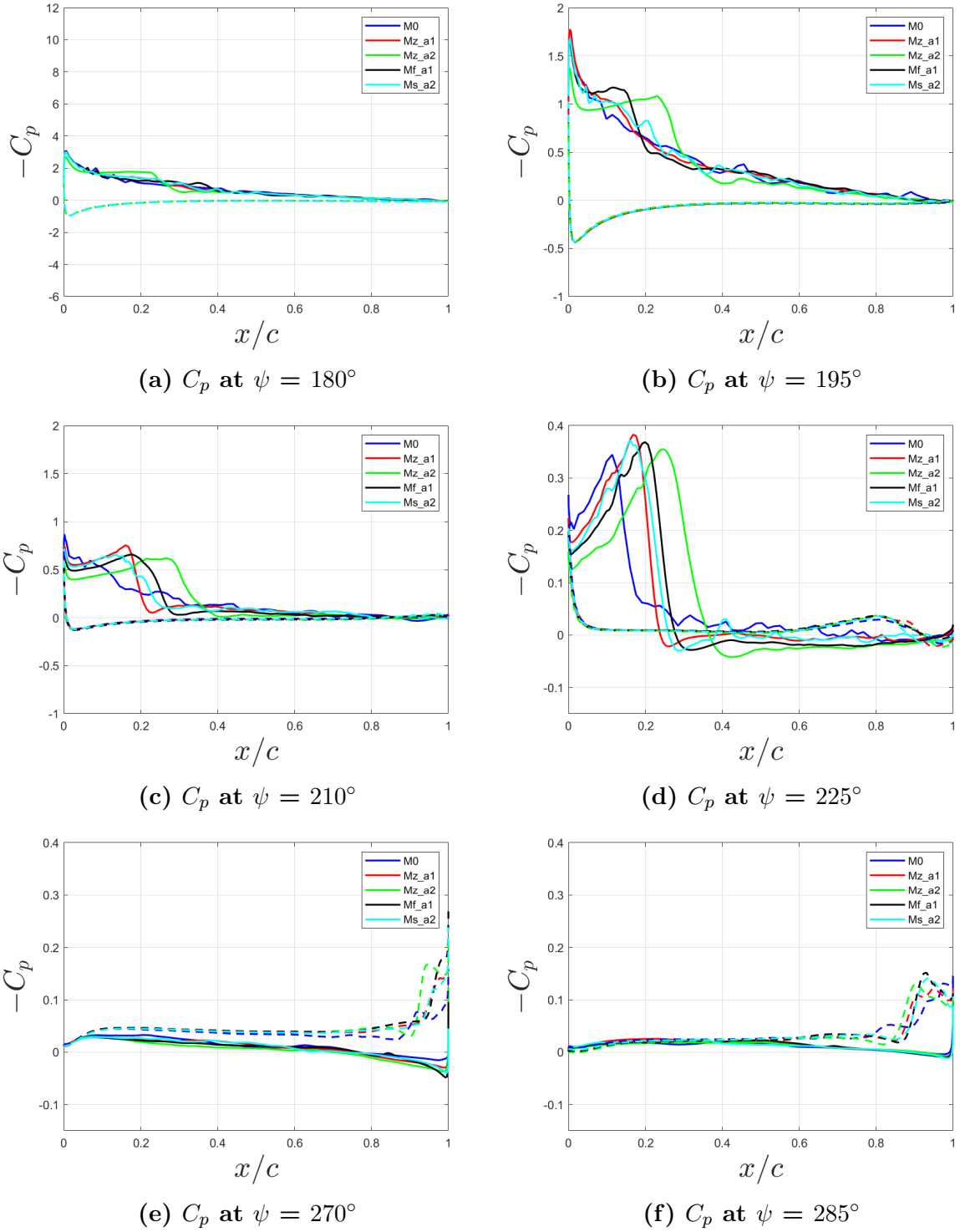


Figure 4.20: C_p comparison for different meshes. Top surface C_p is denoted by solid lines and bottom surface C_p is denoted by dashed lines

In summary, mesh refinement/adaptation is necessary to perform accurate LES of

complex aerodynamic problems.

CHAPTER 5

Results and Discussion: Zonal Based Adaptation/Refinement

In this section, we focus on adaptive LES of flow over a surging airfoil at

5.1 Force Response

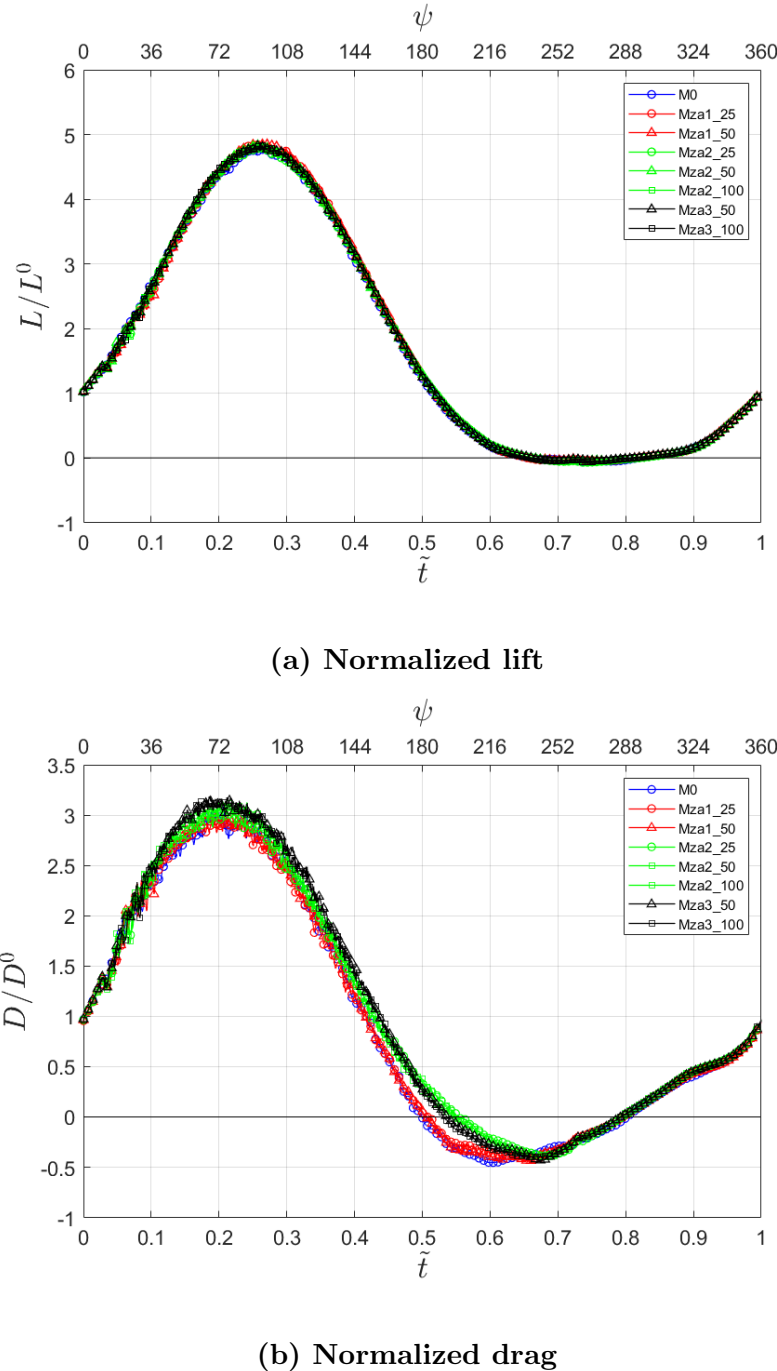


Figure 5.1: Normalized forces for different meshes

5.2 Flowfield: Spanwise Vorticity

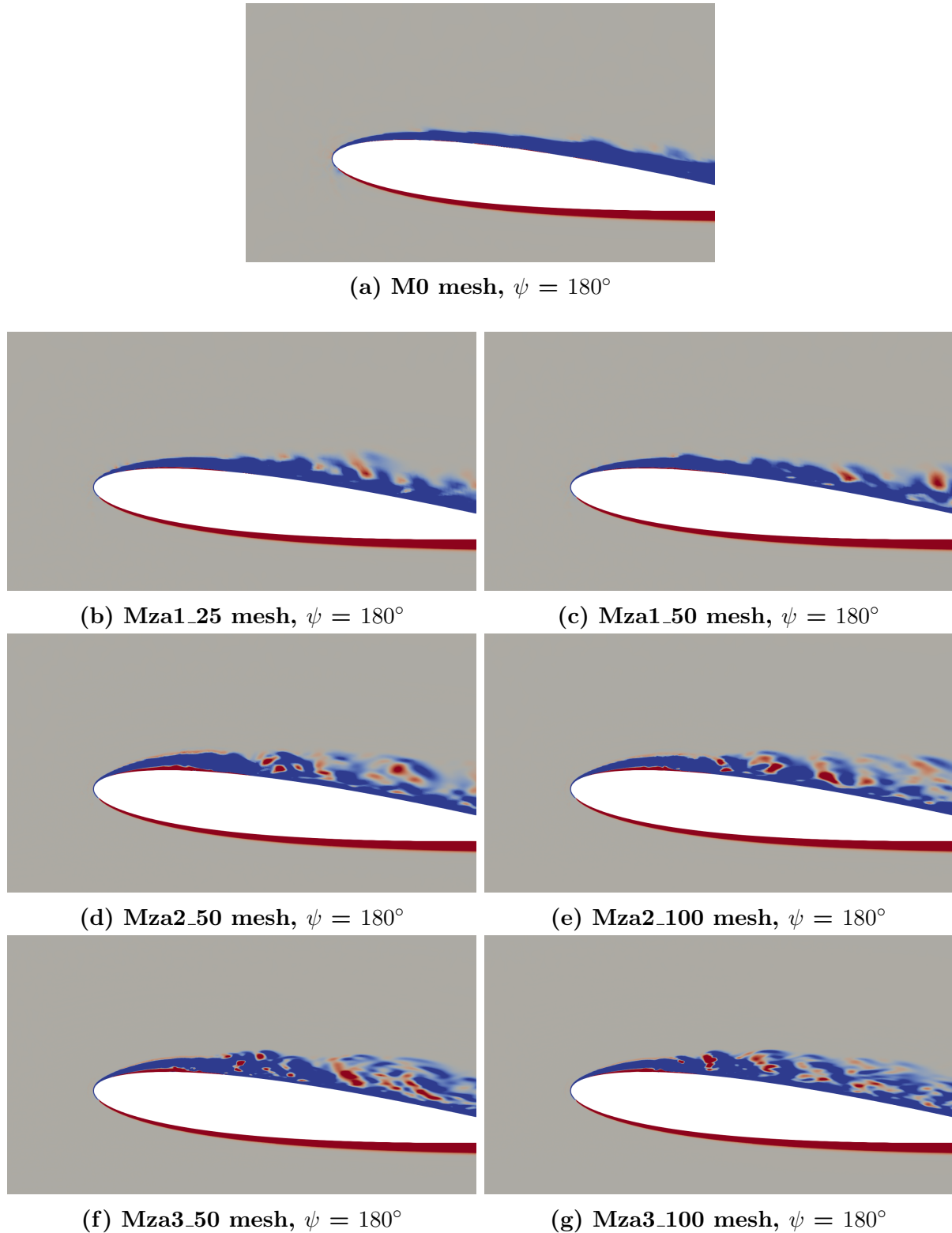


Figure 5.2: Spanwise vorticity comparison at $\psi = 180^\circ$ for different meshes

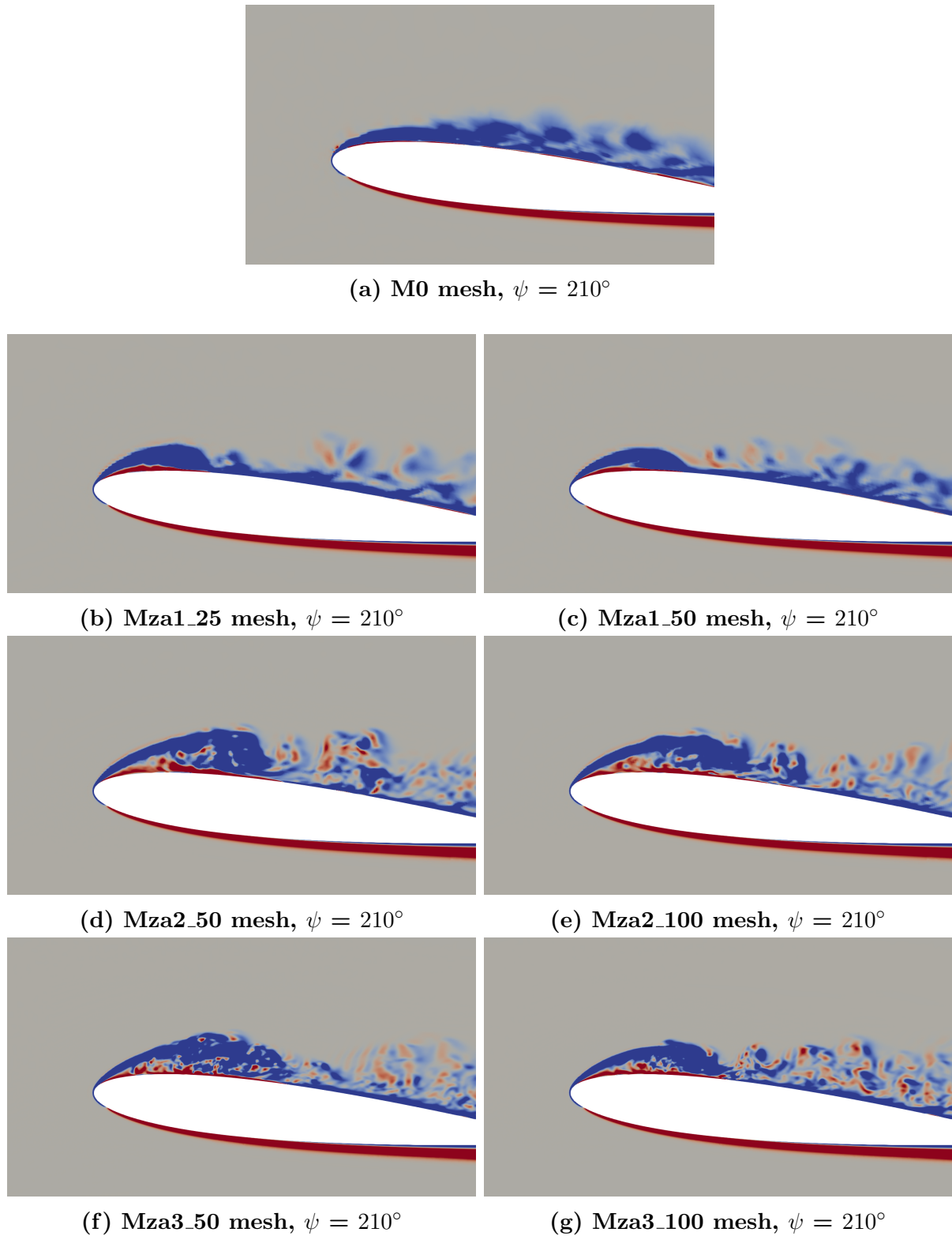


Figure 5.3: Spanwise vorticity comparison at $\psi = 210^\circ$ for different meshes

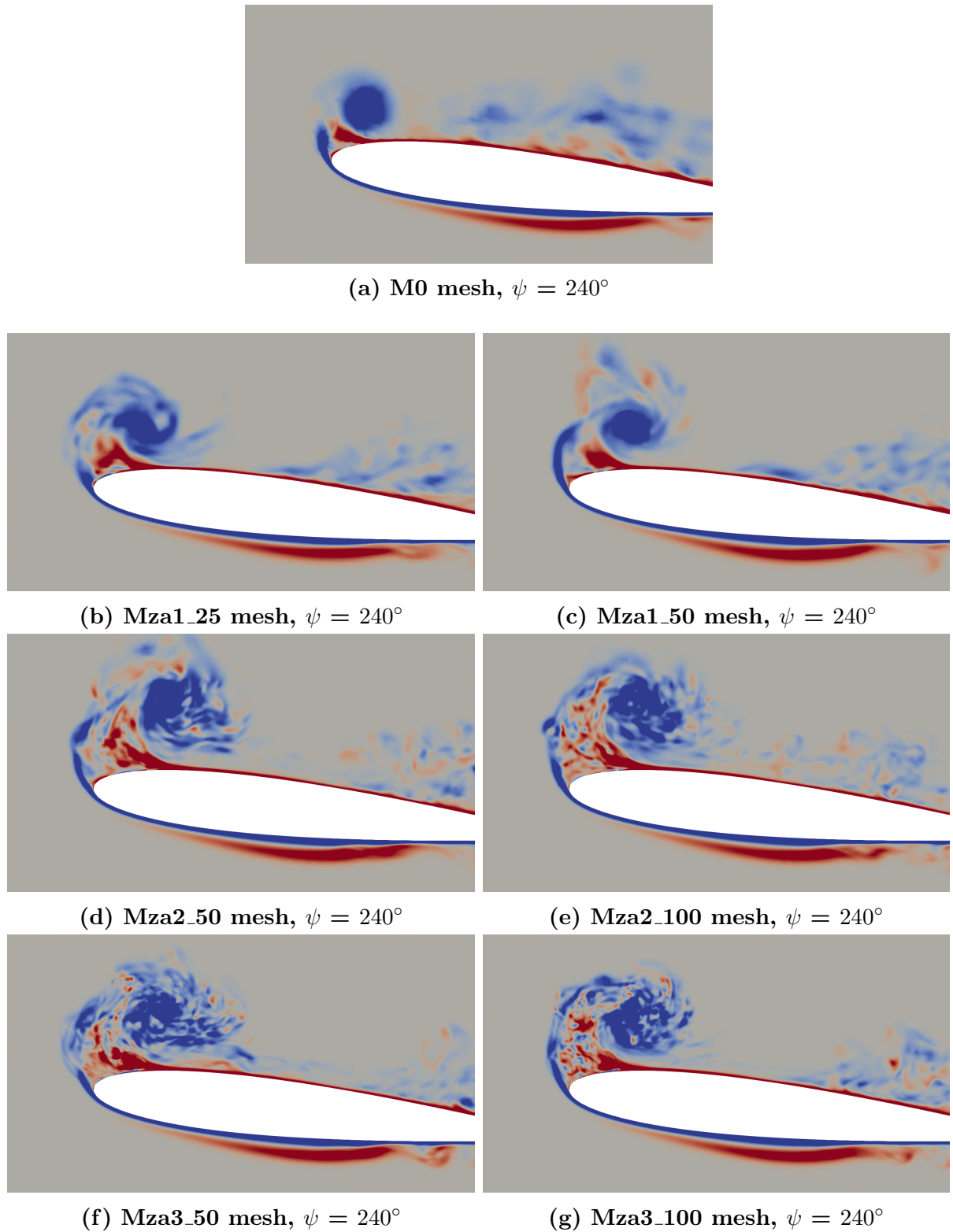


Figure 5.4: Spanwise vorticity comparison at $\psi = 240^\circ$ for different meshes

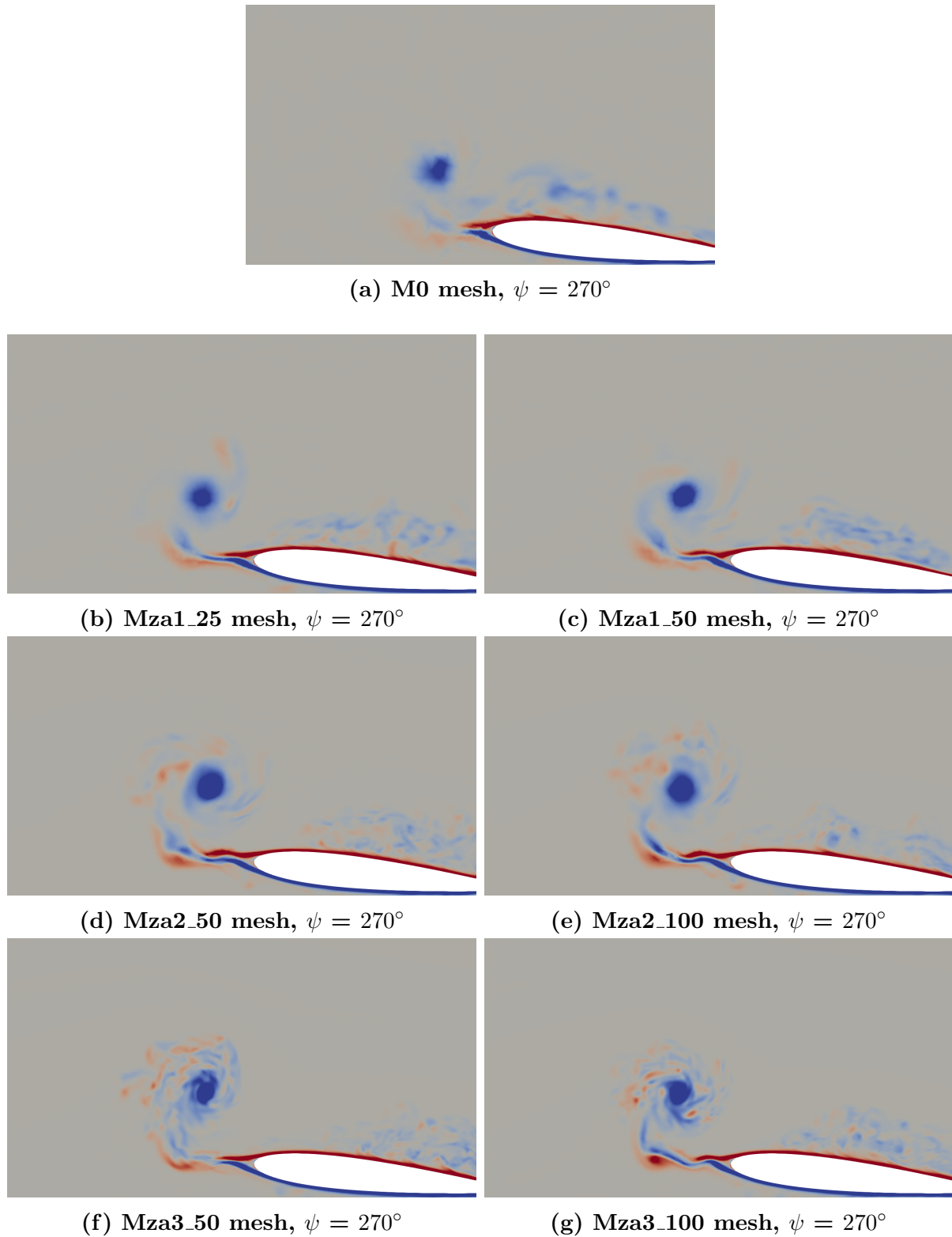
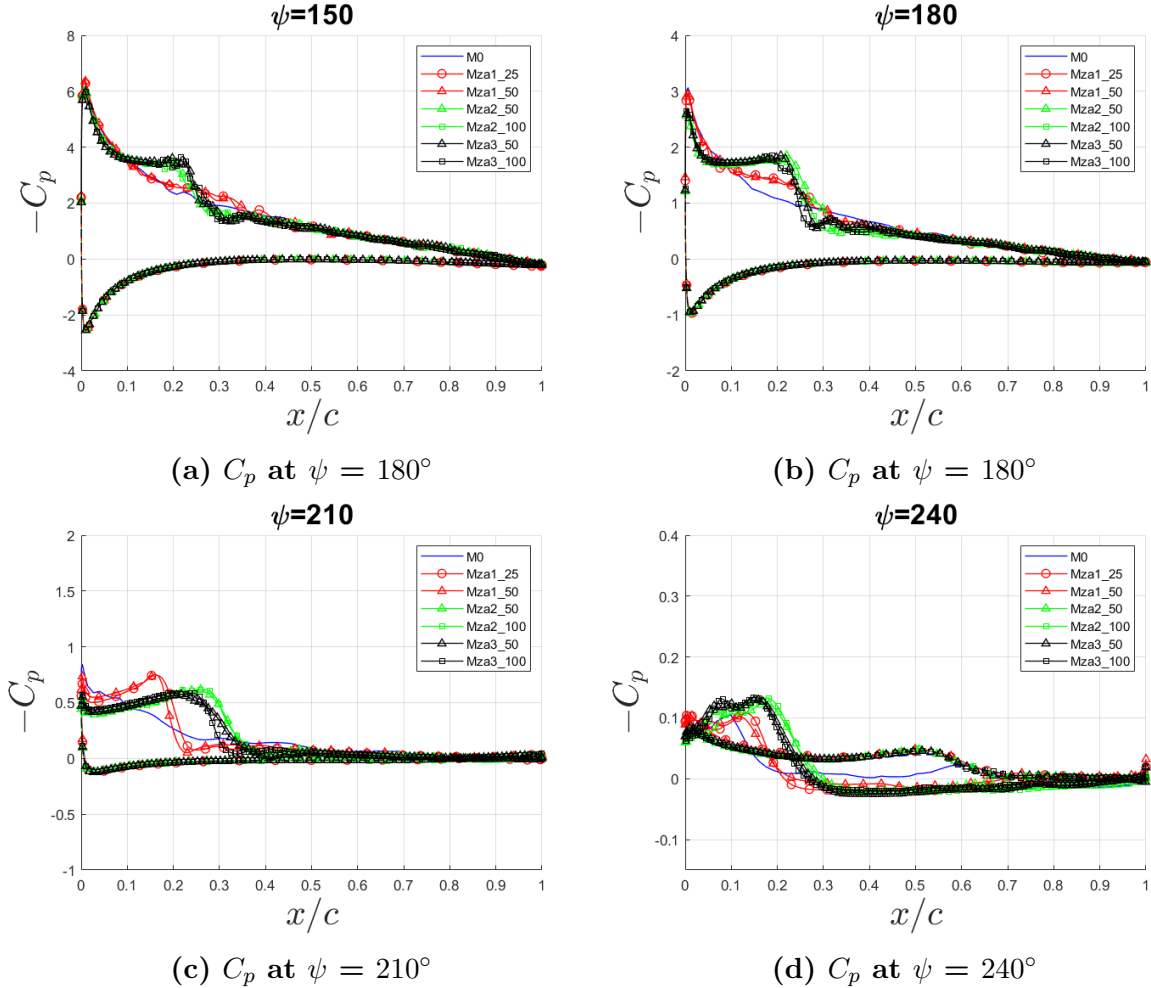


Figure 5.5: Spanwise vorticity comparison at $\psi = 270^\circ$ for different meshes

5.3 Cp

5.3.1 Cp: LEV



5.3.2 Cp: Trailing Edge Separation

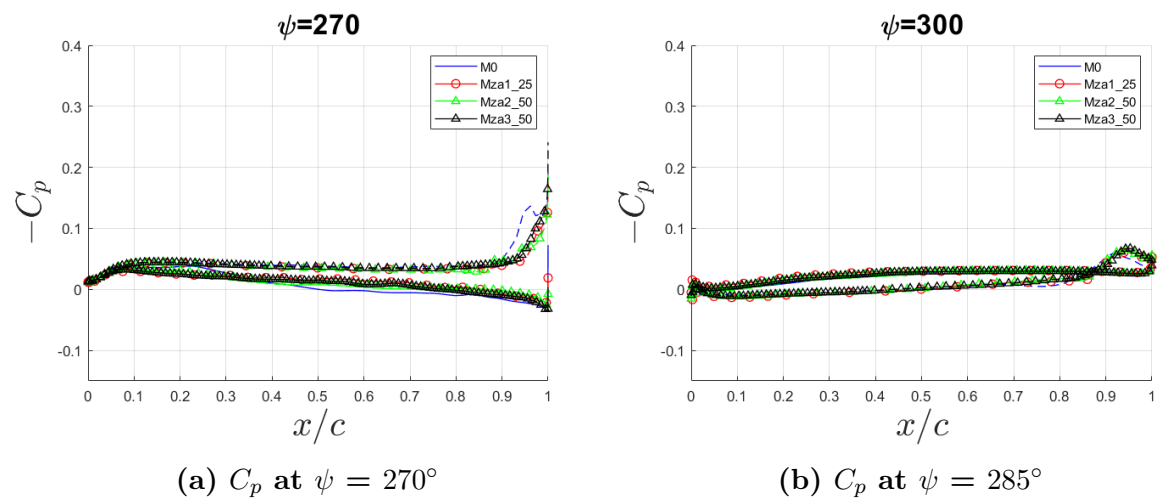


Figure 5.7: C_p comparison for different meshes. Top surface C_p is denoted by solid lines and bottom surface C_p is denoted by dashed lines

APPENDIX A
THIS IS AN APPENDIX